The Astrophysical Journal, 642:673–693, 2006 May 10

CHANDRA AND *SPITZER* UNVEIL HEAVILY OBSCURED QUASARS IN THE *CHANDRA*/SWIRE SURVEY[1]

Maria del Carmen Polletta,[2] Belinda J. Wilkes,[3] Brian Siana,[4,5] Carol J. Lonsdale,[2,6] Roy Kilgard,[3] Harding E. Smith,[2,5] Dong-Woo Kim,[3] Frazer Owen,[5,7] Andreas Efstathiou,[8] Tom Jarrett,[6] Gordon Stacey,[9] Alberto Franceschini,[10] Michael Rowan-Robinson,[11] Tom S. R. Babbedge,[11] Stefano Berta,[10] Fan Fang,[4] Duncan Farrah,[9] Eduardo González-Solares,[12] Glenn Morrison,[5,13] Jason A. Surace,[4] and Dave L. Shupe[4]

Received 2005 September 10; accepted 2005 December 21

ABSTRACT

Using the large multiwavelength data set in the *Chandra*/SWIRE Survey (0.6 deg^2 in the Lockman Hole), we show evidence for the existence of highly obscured (Compton-thick) AGNs, estimate a lower limit to their surface density, and characterize their multiwavelength properties. Two independent selection methods based on the X-ray and infrared spectral properties are presented. The two selected samples contain (1) five X-ray sources with hard X-ray spectra and column densities $\gtrsim 10^{24}$ cm^{-2} and (2) 120 infrared sources with red and AGN-dominated infrared SEDs. We estimate a surface density of at least 25 Compton-thick AGNs deg^{-2} detected in the infrared in the *Chandra*/SWIRE field, of which $\sim$40% show distinct AGN signatures in their optical/near-infrared SEDs, the remaining being dominated by the host galaxy emission. Only $\sim$33% of all Compton-thick AGNs are detected in the X-rays at our depth [$F(0.3-8$ keV$) > 10^{-15}$ ergs cm^{-2} s^{-1}]. We report the discovery of two sources in our sample of Compton-thick AGNs, SWIRE J104409.95+585224.8 ($z = 2.54$) and SWIRE J104406.30+583954.1 ($z = 2.43$), which are the most luminous Compton-thick AGNs at high z currently known. The properties of these two sources are discussed in detail with an analysis of their spectra, SEDs, luminosities, and black hole masses.

Subject headings: galaxies: active — infrared: galaxies — quasars: individual (SWIRE J104409.95+585224.8, SWIRE J104406.30+583954.1) — X-rays: galaxies

Online material: extended figure, machine-readable table

1. INTRODUCTION

According to the active galactic nucleus (AGN) unification models (Antonucci 1993; Krolik 1999), all AGNs are intrinsically similar, and the observational differences among various types are due to the geometry and orientation with respect to the line of sight of obscuring matter surrounding the central supermassive black hole (SMBH). According to this model, obscuring matter is ubiquitous in AGNs, but the effects of absorption are only seen when the line of sight intercepts it. Alternative models attribute the presence of obscuration to a stage in the early phases of AGN evolution during a merger (Fabian 1999). Mergers of large disk galaxies hosting an SMBH induce the growth of the SMBH and of the host galaxy spheroid throughout vigorous star formation episodes. During this phase the AGN is surrounded by large amounts of gas and dust; thus, it appears as heavily obscured. As the AGN reaches a certain luminosity, its radiation can cause the expulsion and destruction of the surrounding material and the system appears as an unobscured AGN (Silk & Rees 1998; Granato et al. 2004; Springel et al. 2005; Hopkins et al. 2005; Di Matteo et al. 2005; Cattaneo et al. 2005).

Since AGNs that are not affected by obscuration are relatively easy to detect and identify across the entire wavelength spectrum, they have been well sampled up to high redshifts and their properties, space density, luminosity function, and redshift distributions are well measured (Ueda et al. 2003; Richards et al. 2005). On the other hand, AGNs obscured by even only moderate column densities ($N_{\rm H} \simeq 10^{22}$ cm^{-2}; Richards et al. 2003; White et al. 2003) are routinely missed in observations at various wavelengths because of the difficulty of detecting and identifying them; therefore, they are not as well understood. There is evidence that

[1] Some of the data presented herein were obtained at the W. M. Keck Observatory, which is operated as a scientific partnership among the California Institute of Technology, the University of California, and the National Aeronautics and Space Administration. The Observatory was made possible by the generous financial support of the W. M. Keck Foundation. Based on observations at the Kitt Peak National Observatory, National Optical Astronomy Observatory, which is operated by the Association of Universities for Research in Astronomy, Inc., under cooperative agreement with the National Science Foundation. The National Radio Astronomy Observatory is a facility of the National Science Foundation operated under a cooperative agreement by Associated Universities, Inc.

[2] Center for Astrophysics and Space Sciences, University of California, San Diego, 9500 Gilman Drive, La Jolla, CA 92093-0424.

[3] Harvard-Smithsonian Center for Astrophysics, 60 Garden Street, Cambridge, MA 02138.

[4] *Spitzer* Science Center, California Institute of Technology, 100-22, 1200 East California Boulevard, Pasadena, CA 91125.

[5] Visiting Astronomer, Kitt Peak National Observatory, National Optical Astronomy Observatory, operated by AURA, Inc., under cooperative agreement with the National Science Foundation.

[6] Infrared Processing and Analysis Center, California Institute of Technology, 100-22, Pasadena, CA 91125.

[7] National Radio Astronomy Observatory, P.O. Box O, 1003 Lopezville Road, Socorro, NM 87801.

[8] School of Computer Science and Engineering, Cyprus College, 6 Diogenes Street, Engomi, 1516 Nicosia, Cyprus.

[9] Department of Astronomy, Cornell University, 610 Space Sciences Building, Ithaca, NY 14853.

[10] Dipartimento di Astronomia, Universitá di Padova, Vicolo dell'Osservatorio 2, I-35122 Padova, Italy.

[11] Astrophysics Group, Blackett Laboratory, Imperial College, Prince Consort Road, London SW7 2BW, UK.

[12] Institute of Astronomy, University of Cambridge, Madingley Road, Cambridge CB3 0HA, UK.

[13] Institute for Astronomy, University of Hawaii, 2680 Woodlawn Drive, Honolulu, HI 96822; and Canada-France-Hawaii Telescope, 65-1238 Mamalahoa Highway, Kamuela, HI 96743-8432.

obscured AGNs are numerous and might even outnumber unobscured AGNs; however, optically and X-ray–selected samples of AGNs are still dominated by unobscured AGNs, and large and complete samples of obscured AGNs are still missing, providing only few observables to constrain models.

1.1. *Indirect Evidence for the Existence of Highly Obscured AGNs*

In the local universe and for moderate (Seyfert like) nuclear luminosities ($<10^{44}$ ergs s^{-1}), the observed ratio between obscured ($N_{\rm H} > 10^{22}$ cm^{-2}) and unobscured ($N_{\rm H} < 10^{22}$ cm^{-2}) AGNs is 4 : 1 (Osterbrock & Shaw 1988; Madau et al. 1994; Comastri et al. 1995; Risaliti et al. 1999; Piconcelli et al. 2003), and ~45% of the obscured ones are Compton thick (column density larger than 10^{24} cm^{-2}; Risaliti et al. 1999; Maiolino & Rieke 1995). Large column densities ($\sim 10^{24}$ cm^{-2}) have been directly measured only in a few (~10) sources (e.g., NGC 1068, Circinus, NGC 4945). For most of the known Compton-thick AGNs (~40; Comastri 2004), only indirect evidence of their extreme column densities is available (Bassani et al. 1999; Risaliti et al. 1999; Maiolino et al. 2003), such as the flatness of the hard X-ray continuum, a large equivalent width (EW) of the Kα 6.4 keV iron fluorescent emission line, or lower than expected values of the ratio between the flux in the X-rays and in other wavelengths. At higher redshift (>1) and luminosities ($\geq 10^{44}$ ergs s^{-1}), the distribution of absorption in AGNs is not as well constrained, with only a few examples of confirmed obscured quasars. There is evidence that the fraction of obscured AGNs decreases with higher intrinsic luminosities (Ueda et al. 2003; Szokoly et al. 2004; Barger et al. 2005; Treister & Urry 2005) and possibly increases with redshift (La Franca et al. 2005).

Other indications for the existence of numerous obscured AGNs have been provided by AGN studies at wavelengths less affected by obscuration, such as infrared (IR) and radio. Stern et al. (2005) compared the surface density of an IR-selected sample of AGNs [$F(8\ \mu{\rm m}) > 76\ \mu$Jy] with that of an optically selected (R-mag < 21; Wolf et al. 2003) sample of AGNs and found 2.8 times more AGNs in the IR than in the optical sample. Since the ratio between the limiting fluxes of the two samples corresponds to the typical R-band/8 μm flux ratio of unobscured AGNs, the higher density of IR-selected AGNs is attributed to an excess of obscured AGNs. Similar results were obtained from an IR- and radio-selected sample of AGNs (Martínez-Sansigre et al. 2005) in which the fraction of obscured sources at high redshift ($z \sim 2$) is estimated to be 50% (obscured : unobscured = 1 : 1), or as high as 87% (obscured : unobscured = 2.6 : 1) if sources that are not confirmed spectroscopically are also taken into account. An obscured : unobscured ratio of 2 : 1 was also derived from a sample of AGNs selected at 24 μm (Alonso-Herrero et al. 2006).

The existence of a large population of obscured AGNs is also suggested by the shape of the X-ray background at high energies. More than 85% of the 2–10 keV cosmic X-ray background (CXRB) has been resolved by sources detected in deep X-ray surveys (Moretti et al. 2003; De Luca & Molendi 2004). However, the resolved fraction decreases at higher energies, e.g., in the 4–6 keV energy range the resolved fraction is about 70%–90%, while in the 8–12 keV band no more than 50% is resolved. Less than 30% is resolved above 10 keV, where the bulk of the CXRB energy density is produced (Worsley et al. 2004, 2005). The spectral shape of the residual background cannot be produced by a simple superposition of unobscured AGN spectra, but by an X-ray population with faint low-energy X-ray fluxes and hard X-ray spectra, as in obscured AGNs (Worsley et al. 2005).

1.2. *Searches for Obscured AGNs*

In spite of the difficulty of finding and identifying highly obscured AGNs, several searches have been conducted combining multiwavelength data (Webster et al. 1995; Wilkes et al. 2002; Padovani et al. 2004; Donley et al. 2005; Stern et al. 2005; Martínez-Sansigre et al. 2005; Zakamska et al. 2004; Urrutia et al. 2005), performing very deep observations (Treister & Urry 2005; Van Duyne et al. 2004), or surveying large areas of the sky (Cutri et al. 2002; Fiore et al. 2003; Zakamska et al. 2004; Urrutia et al. 2005). Obscured AGN candidates have been selected among X-ray sources with hard X-ray spectra or with high (>10) X-ray/optical flux ratios (Fiore et al. 2003; Rigby et al. 2004), with radio emission in excess compared to the IR (Donley et al. 2005; Urrutia et al. 2005) or with narrow emission lines in their optical spectra (Zakamska et al. 2004). These sources are predominantly characterized by column densities of the order of 10^{22} cm^{-2} and by various types of optical spectra, with narrow emission lines as expected in type 2 AGNs, but also with broad emission lines, as in unobscured AGNs, or typical of normal, early- and late-type galaxies (Fiore et al. 2003; Perola et al. 2004).

All of these studies aimed at finding the obscured AGN population predicted by models, and indirect observations have been successful to varying degrees. However, most of these samples are affected by selection effects and characterized by properties too broad to constrain models, and the measured column densities are only moderate ($N_{\rm H} = 10^{22}-10^{23}$ cm^{-2}). A common property of these moderately obscured AGNs is the variety of optical/near-IR spectral energy distributions (SEDs), with only a minority of sources showing typical AGN signatures (Franceschini et al. 2005; Donley et al. 2005; Rigby et al. 2004). Consequently, any search in a specific wavelength range will provide incomplete samples of obscured AGNs.

In this work, we aim at identifying and characterizing only the most obscured AGNs, with columns densities of the order of 10^{24} cm^{-2}, the so-called Compton-thick AGNs. By looking at the most obscured AGNs, which are also the hardest to find because of their elusive properties, we hope to provide useful constraints on AGN models. Our analysis is based on the sources detected by *Spitzer* and *Chandra* in a wide-area (0.6 deg^2) multiwavelength (from radio to X-ray) survey performed in the Lockman Hole, the *Chandra*/SWIRE survey. This field was selected for deep follow-up observations within the *Spitzer* Wide-Area Infrared Extragalactic (SWIRE) survey (Lonsdale et al. 2003, 2004) legacy project. By comparing samples selected independently in the X-rays and in the IR, the incompleteness level of each selection method can be estimated. The available multiwavelength data set is described in § 2. We present our selection methods for heavily obscured AGNs in § 3, an X-ray–based selection in § 3.1, and an IR-based selection in § 3.2. The general properties of the two samples, SEDs, and X-ray/optical and X-ray/mid-IR fluxes are discussed in §§ 3.2.2 and 3.2.3. A detailed analysis of the properties of two spectroscopically confirmed Compton-thick quasars present in both samples is given in §§ 4 (data description), 5 (SED analysis), and 6 (bolometric luminosity and black hole mass estimate). A comparison between our candidates and other samples of heavily obscured AGNs is presented in § 7. In § 8 we estimate a lower limit to the surface density of Compton-thick AGNs detected in the IR at our sensitivity limits in the *Chandra*/SWIRE field and compare

TABLE 1
SUMMARY OF OBSERVATIONS IN THE *Chandra*/SWIRE SURVEY

Telescope/Instrument	$\alpha_{J2000.0}$	$\delta_{J2000.0}$	Area[a]	Observing Date	Band	Exposure Time (s)	5 σ Limit (μJy/Vega mag)
KPNO: Mayall 4 m/Mosaic.....	10 46	+59 00	30 × 30	2004 Jan	U	21600	24.8
	10 46	+59 03	60 × 54	2004 Jan	U	7200	24.3
	10 46	+59 00	30 × 30	2002 Feb	g', r', i'	10800	25.9, 25.2, 24.4
	10 46	+59 03	60 × 54	2002 Feb	g', r'	3000	25.2, 24.4
	10 46	+59 03	60 × 54	2002 Feb	i'	1800	23.5
	10 46	+58 33	60 × 6	2002 Feb	g', r', i'	1800	23.7, 23.5, 22.9
Palomar: 200″ Hale/WIRC	10 46	+59 00	36 × 43	2004 Mar 29	K_s	4320	20.5
VLA	10 46	+59 01	40 × 40	2001, 2002, and 2003	20 cm	500000	13.5
Chandra/ACIS-I.....	10 46	+59 01	47 × 47	2004 Sep 12–26	0.3–8 keV	70000	10^{-15}[b]
Spitzer/IRAC.....	10 45	+58 00	3.69 × 3.01	2003 Dec and 2004 Apr	3.6, 4.5, 5.8, 8.0 μm	120–480	5, 9, 43, 40
Spitzer/MIPS.....	10 45	+58 00	3.66 × 3.00	2003 Dec and 2004 May	24 μm	160–360	230

NOTE.—Units of right ascension are hours and minutes, and units of declination are degrees and arcminutes.
[a] For the values given in the final two rows, units are degrees; for all other values, units are arcminutes.
[b] Units are ergs cm^{-2} s^{-1}.

our estimates with current models. Our results are summarized in § 9.

Throughout the paper we adopt a flat cosmology with $H_0 = 71$ km s^{-1} Mpc^{-1}, $\Omega_M = 0.27$, and $\Omega_\Lambda = 0.73$ (Spergel et al. 2003).

2. OBSERVATIONS

The *Chandra*/SWIRE field, located in the northern part of the Lockman Hole field (10^h45^m, +59°), has been selected as the target for the deepest IR, optical, and radio SWIRE observations and for a moderately deep and wide *Chandra* survey. This field has the lowest cirrus sky emission of all of the SWIRE fields (0.38 MJy sr^{-1} at 100 μm) and has no contamination from moderate brightness radio sources, making it ideally suited for a radio–IR survey. The neutral Galactic column density toward this field is on average 6.43×10^{19} cm^{-2} (Dickey & Lockman 1990), making it ideal also for deep X-ray surveys. The data available in this field are summarized in Table 1, and details on the observations are given in the following sections.

2.1. *Optical and Infrared Imaging Observations*

Optical imaging in U, g', r', and i' was obtained with the Mosaic Camera at the Kitt Peak National Observatory (KPNO) Mayall 4 m Telescope on 2002 February (g', r', and i') and 2004 January (U). The coverage of the field is not uniform; the central 0.3 deg^2 ($\alpha = 161°-162°$ and $\delta = 58.°75-59.°25$) were covered with a 3 hr exposure in g', r', and i' and with a 6 hr exposure in U band to 5 σ limiting Vega magnitudes of 24.8 (U), 25.9 (g'), 25.2 (r'), and 24.4 (i'). The surrounding area at $\delta > 58.°6$ was also covered in four bands with a 50 minute exposure in g' and r', a 30 minute exposure in i', and a 2 hr exposure in U band to a depth of 24.3 (U), 25.2 (g'), 24.4 (r'), and 23.5 (i'). The small region at $\delta < 58.°6$ was observed only in the g', r', and i' bands with a 30 minute exposure to a depth of 23.7 (g'), 23.5 (r'), and 22.9 (i'). The astrometry is good to less than 0.″4, and the seeing varies between 0.″9 and 1.″4. The data were processed with the Cambridge Astronomical Survey Unit's reduction pipeline following the procedures described in Babbedge (2004). Fluxes were measured within 3″ apertures (diameter) and corrected to total fluxes using profiles measured on bright stars. Total magnitudes, derived by integrating over the curve of growth, were adopted for sources extended and bright in the three filters g', r', and i' ($g' < 23.8, r' < 22.7, i' < 22.0$). The optical catalog contains 77,355 sources (galaxies and stars), of which 45,573 are detected in at least two bands.

Near-IR K_s imaging observations were carried out with the 200″ Hale Telescope of the Palomar Observatory using the Wide Infrared Camera (WIRC; Wilson et al. 2003) on 2004 March 29 under photometric conditions. The field was partially covered, 0.43 deg^2, with 24 8.′5 × 8.′5 pointings of 72 minute exposure. Data reduction for the near-IR imaging consisted of median-sky removal, flat-fielding using a median "sky" image derived from the science observations, co-addition, and astrometric and flux calibration. The seeing FWHM ranges between 0.″7 and 1.″3. Sources were extracted using SExtractor (Bertin & Arnouts 1996) and MAG_BEST magnitudes were adopted. Calibration was carried out using the near-IR Two Micron All Sky Survey (2MASS) Point Source Catalog (Cutri et al. 2003). The K_s band photometric uncertainty, relative to 2MASS, is ~6% and the 5 σ sensitivity is 20.5 mag (Vega). The K_s catalog contains 19,876 sources, of which 17,140 have an optical counterpart.

Observations with the Infrared Array Camera (IRAC; Fazio et al. 2004) were performed on 2003 December 5 and 2004 April 24–30, and observations with the Multiband Imaging Photometer (MIPS; Rieke et al. 2004) were performed on 2003 December 9 and 2004 May 4–11. The IRAC depth was 120–480 s, depending on exact field location, with a median depth of 240 s, and MIPS depth was 160–360 s, with a median depth of 360 s. Fluxes were measured using SExtractor (Bertin & Arnouts 1996) from mosaics of the flat-fielded images processed by the *Spitzer* Science Center using the S11 data pipelines. Fluxes were extracted in 5.″8 diameter apertures for IRAC (~2–3 times the FWHM beam) and 12″ for MIPS 24 μm using SExtractor (Bertin & Arnouts 1996) and corrected for aperture to total fluxes using the IRAC/MIPS point-spread functions (PSFs). In the case of extended sources (SExtractor stellarity index <0.8 and *ISO* area >200) in the IRAC images, Kron fluxes were used. Details of the IRAC and MIPS data processing are given in Surace et al. (2005). The 5 σ depths of the *Spitzer* data are 5, 9, 43, 40, and 230 μJy at 3.6, 4.5, 5.8, 8.0, and 24 μm, respectively. The IR catalog contains 41,262 sources, of which 31,106 have an optical counterpart.

2.2. *Chandra X-Ray Data and Analysis*

We have obtained *Chandra* Advanced CCD Imaging Spectrometer (ACIS-I; Weisskopf et al. 1996) observations in a 3 × 3 raster of a 0.6 deg^2 region with center $\alpha = 10^h46^m$ and $\delta = +59°01'$ and ~2′ overlap between contiguous pointings within the Lockman Hole field of the SWIRE survey. The exposure

time for each observation was ~70 ks, reaching broadband (0.3–8 keV), soft-band (0.3–2.5 keV), and hard-band (2.5–8 keV) fluxes of $\sim 10^{-15}$, 5×10^{-16}, and 10^{-14} ergs cm^{-2} s^{-1}, respectively. The observations were obtained on 2004 September 12–26 and processed using the XPIPE pipeline developed for analysis of *Chandra* data for the ChaMP project (Kim et al. 2004). XPIPE screens bad data, corrects instrumental effects remaining after the standard pipeline processing, detects the X-ray sources (using `wavdetect` [Freeman et al. 2002] in the CIAO 3.2 software package[14]), and determines counts in the soft (0.3–2.5 keV), hard (2.5–8.0 keV), and broad (0.3–8.0 keV) bands. A false-positive threshold of 10^{-6} in `wavdetect` is used to accept a source, corresponding to roughly one spurious source per ACIS-I chip, or four per field. The background- and exposure-corrected count rates for each source were converted to fluxes using conversion factors computed using XSPEC and assuming a power-law model [$F(E) \propto E^{-(\Gamma-1)} e^{-\sigma(E) N_{\rm H}}$, where E is the energy, $F(E)$ is the flux density, $\sigma(E)$ is the photoelectric cross section (Morrison & McCammon 1983), Γ is the photon index, and $N_{\rm H}$ is the column density associated with the absorbing material] with $\Gamma = 1.7$ and $N_{\rm H} = 6 \times 10^{19}$ cm^{-2}. The analysis of the X-ray data and details on the observations will be presented in a future publication.

A total of 812 sources were detected in the initial analysis. The X-ray source list was cross-correlated with the *Spitzer* source list using a search radius corresponding to the quadratic sum of the *Chandra* positional uncertainty (2″ minimum) and of the IR positional uncertainty that was fixed to 2″. Based on the visual inspection of the images and the low detection reliability, 20 sources are considered to be spurious. This is roughly the number expected since one source per ACIS chip would lead to 27 spurious sources. These X-ray sources were not included in the X-ray catalog for further analysis, reducing the total number of X-ray sources to 792. An IR counterpart is matched to 766 sources, 631 of which are also detected in the optical images. Sixteen sources are detected only in the optical, and 10 X-ray sources do not have either an IR or optical counterpart. The majority of the X-ray sources (561 out of 792 sources or 71%) have a unique optical or IR counterpart within the positional uncertainty, and 213 sources have multiple matches (130 sources have two matches, 49 have three matches, and the remaining 34 have more than three matches). In the case of multiple matches the closest source was chosen as the counterpart, unless there was another candidate at similar distance that was a brighter and redder IR source (10 cases). To estimate the reality of the associations, we calculated the probability of random matches between the X-ray sources and the possible *Spitzer* counterparts following the same procedure discussed in Fadda et al. (2002) and Franceschini et al. (2005), which assumes that the IR population follows a Poisson spatial distribution. Most of the *Chandra* sources with multiple associations are unambiguously identified as the X-ray positional uncertainty is small (~2″) and one counterpart is at less than 0.″5 from the X-ray source and the others are at more than 2″. In eight cases, the positional uncertainties were sufficiently large, i.e., sources at large off-axis angles, to have several possible matches. The closest source was selected; however, the reliability of these matches is very low. Approximately 88% have a probability of random matches $P < 5\%$. Summing the probabilities, we expect about 19 false associations in the 774 matched sources. Eighteen of the 774 matched sources are close to bright sources, mostly stars, and therefore do not have reliable optical and IR photometric measurements.

[14] *Chandra* Interactive Analysis of Observations (CIAO), http://cxc.harvard.edu/ciao.

2.3. *Radio Imaging*

A deep, 1.4 GHz radio map centered at $\alpha = 10^{\rm h}46^{\rm m}$, $\delta = +59^\circ 01'$ and covering $40' \times 40'$ in the *Chandra*/SWIRE field was obtained at the Very Large Array (VLA) during multiple dates, 2001 December 15, 2002 January–March, and 2003 January 6 (F. Owen et al. 2006, in preparation). VLA configurations A/B/C and D were used. The total integration time spent on source was 500 ks. The rms noise in the center of the radio image is 2.7 μJy. The source density decreases at larger distances from the center of the field, from about 9400 sources deg^{-2} within 10′ from the center (~4.5 μJy rms) to about 4300 sources deg^{-2} at a distance between 10′ and 20′, and less than 1000 sources deg^{-2} at a distance greater than 20′ (~16 μJy rms). There are 2052 radio sources in the entire field, and 2000 are also detected in the IR with IRAC. The fraction of IR sources that are detected at radio wavelengths varies from 13% within 10′ from the center of the radio field to about 7% in the entire radio field. The fraction of X-ray sources that are radio detected is almost 4 times higher than the fraction of radio-detected IR sources, with 50% of all X-ray sources within 10′ from the center and 27% in the whole field.

2.4. *Optical Spectroscopy*

Spectroscopic observations were carried out using various facilities, with Hydra on the WIYN Observatory on 2004 February 11–15, with the Low Resolution Imaging Spectrometer (LRIS; Oke et al. 1995) on the Keck I telescope on 2004 February 24–25 and 2005 March 3–4, and with the Gemini Multi-Object Spectrograph (GMOS) on the Gemini Observatory on 2004 February 21–23. Details on these observations will be published in a future publication (H. Smith et al. 2006, in preparation). Details on the Keck observations are given in § 4.1. Spectroscopic redshifts from the Sloan Digital Sky Survey[15] (SDSS) are also available. In total, spectroscopic redshifts are available for 574 IR sources, of which 74 are also X-ray sources, 48 from Keck, 81 from Gemini, 412 from WIYN, and 35 from SDSS.

The IR, X-ray, and radio source lists and the matched multiwavelength catalogs will be presented in future publications (M. Polletta et al. 2006, in preparation; F. Owen et al. 2006, in preparation).

3. SELECTION OF OBSCURED AGN CANDIDATES

In the following sections we present two methods for selecting AGNs with extreme column densities ($N_{\rm H} \gtrsim 10^{24}$ cm^{-2}), the so-called Compton-thick AGNs: one based on the X-ray properties and one based on the optical–IR properties. Since the methods require knowing the redshift, and spectroscopic redshifts are available for only a small fraction of sources, we supplement the spectroscopic redshifts with photometric redshifts. Photometric redshifts were derived using the code HyperZ (Bolzonella et al. 2000). HyperZ measures photometric redshifts by finding the best fit, defined by the χ^2 statistic, to the observed SED with a library of galaxy templates. We use 24 galaxy templates that represent normal galaxies (9), starbursts (3), and AGNs (12) and cover the wavelength range from 1000 Å to 500 μm (M. Polletta et al. 2006, in preparation). The same method and template library have been used to fit the SEDs of a sample of X-ray–detected AGNs in the ELAIS-N1 field (Franceschini et al. 2005).

3.1. *X-Ray–selected Compton-thick AGNs*

Compton-thick AGNs can show a variety of X-ray spectra, soft and hard, according to the amount of absorption and reflection

[15] See http://www.sdss.org.

TABLE 2
PROPERTIES OF X-RAY–SELECTED COMPTON-THICK AGNs

Source Name	$\alpha_{J2000.0}$[a] (deg)	$\delta_{J2000.0}$[a] (deg)	mag (r') (Vega)	$F_{3.6\,\mu m}$ (μJy)	$F_{4.5\,\mu m}$ (μJy)	$F_{5.8\,\mu m}$ (μJy)	$F_{8.0\,\mu m}$ (μJy)	$F_{24\,\mu m}$ (μJy)	$F_{20\,cm}$ (μJy)
SWIRE J104311.22+591128.2	160.79675	59.191170	22.81	20	20	<43	<40	<230	<87
SWIRE J104322.07+590648.7	160.84196	59.113541	24.83	26	29	<43	<40	<230	64±17
SWIRE J104406.30+583954.1	161.02626	58.665039	23.35	53	67	131	244	1099	<162
SWIRE J104407.67+584011.3	161.03194	58.669800	>25.2	30	34	<43	<40	<230	<154
SWIRE J104409.95+585224.8	161.04146	58.873550	23.55	65	152	401	1082	4011	273±15

NOTE.—Typical uncertainties to the IR fluxes are around 10% of the measured fluxes and to the optical magnitudes are around 0.04 mag. Upper limits correspond to 5 σ.
[a] IR coordinates.

components (Smith & Done 1996; Matt et al. 2000). Therefore, soft X-ray spectra do not necessarily imply low or lack of absorption. However, hard X-ray spectra and X-ray luminosities greater than 10^{42} ergs s^{-1} can be only explained by presence of absorption and can, therefore, be used to identify obscured AGNs.

In this work we select sources with hard X-ray spectra and estimated column densities of the order of 10^{24} cm^{-2}. This method is biased against Compton-thick AGNs in which the primary radiation is completely obscured at the observed energies (<8 keV) and only the warm scattered component is observed that produces soft X-ray spectra. This selection effect is less important for high-z sources where the observed radiation is emitted at higher energies in the source rest frame, which are less affected by obscuration, e.g., for a column density of 10^{24} cm^{-2} the observed flux between 0.3 and 8 keV is reduced by about 98% at $z \sim 0$ and by 71% at $z = 2$ assuming a photon index $\Gamma = 1.7$. Since most of the X-ray sources in the sample are too faint (75% of the sample has less than 50 broadband X-ray counts) to perform full spectral fitting, the amount of absorption is estimated by comparing the counts in the hard and soft X-ray bands. Previous studies (Dwelly et al. 2005; Mainieri et al. 2002; Della Ceca et al. 2004; Perola et al. 2004) have shown that color-based analyses are effective in deriving the properties of X-ray sources with few counts.

Hardness ratios (HRs), defined as $(H - S)/(H + S)$, where H corresponds to the X-ray counts in the hard band (2.5–8 keV) and S to the X-ray counts in the soft band (0.3–2.5 keV), were derived from the observed counts for all of the sources. In order to derive the corresponding absorption, Sherpa (Freeman et al. 2001) simulations were performed for each source assuming an absorbed power-law model. The power-law slope was fixed to a conservative (in terms of N_H estimate) $\Gamma = 1.7$ value, corresponding to the observed mean for AGNs (Nandra & Pounds 1994), and the column density varied from $N_H = 10^{19}$ to $10^{24.5}$ cm^{-2}. The Bayesian method (van Dyk et al. 2004) was applied to take into account the differences in effective area across the detector by estimating the local background for each source. Each spectrum was used as input to MARX[16] to create a simulated data set. HRs were calculated from the simulations of each source and the corresponding N_H were tabulated. The tabulated values were then used to determine the N_H by comparison with the observed HR. In order to derive the effective hydrogen column density, N_H^{rest}, the measured N_H was corrected for the redshift of the source taking into account the energy dependence of the photoelectric cross section (Morrison & McCammon 1983), $N_H^{rest} = N_H^{obs}(1 + z)^{2.6}$ (Barger et al. 2002; Longair 1992). Photometric redshifts were used when spectroscopic redshifts were not available.

[16] See http://space.mit.edu/CXC/MARX.

We found 10 X-ray sources with an intrinsic $N_H^{rest} \gtrsim 10^{24}$ cm^{-2} as derived from the observed HR, assuming spectroscopic redshifts when available and photometric redshifts for the others. Photometric redshifts are still preliminary as more spectroscopic redshifts are being collected and improvements are being implemented. Currently, the total rms for the whole sample of 574 sources with spectroscopic redshifts is 0.26 in $1 + z$, the rate of outliers [defined by $|z_{phot} - z_{spec}|/(1 + z_{spec}) \geq 0.2$] is 8%, and the rms obtained after removing the outliers is 0.08. Although these values are consistent with those derived in other samples of galaxies and AGNs (Babbedge et al. 2004), the uncertainties are still quite large. Therefore, after the selection based on the best photometric redshift, we examined all of the possible solutions obtained by fitting the observed SED with various templates and redshifts. After comparing the reduced χ^2_ν of all solutions with the χ^2_ν given by the best-fit solution, χ^2_ν(best), we removed four sources with secondary solutions with $\chi^2_\nu < 2 \times \chi^2_\nu$(best) at a redshift below the value required to have an $N_H^{rest} = 10^{24}$ cm^{-2}. Another source was removed because of poor optical and IR photometric data due to a bright nearby star that did not allow a reliable fit. The final X-ray–selected sample of obscured AGN candidates contains five sources. Their basic properties (coordinates, r'band magnitudes, IR and radio fluxes) are reported in Table 2, their X-ray properties (broadband, soft-band, and hard-band X-ray fluxes, redshifts, column densities, and absorption-corrected broadband luminosities) are listed in Table 3, and their SEDs are shown in Figure 1.

Two sources show SEDs dominated by AGN emission. Spectroscopic data are also available for these two sources and show narrow emission lines typical of type 2 AGNs. A detailed analysis of the SEDs of these two sources is presented in §§ 4 and 5. The SEDs of the other three sources are dominated by starlight in the optical and near-IR and are best fitted with spiral galaxy templates. The estimated redshifts range from 1.4 to 2.5, the column densities range from 1.0×10^{24} to 9×10^{24}, and the absorption-corrected X-ray (0.3–8 keV) luminosities range from 2.5×10^{45} to 9.5×10^{45} ergs s^{-1}, implying that these are all Compton-thick quasars.

3.2. *IR-selected Obscured AGNs*

Since Compton-thick AGNs might be too faint in the X-rays to be detected at our sensitivity level, we need a complementary selection method that can be applied to the entire IR sample independently of their X-ray data.

In obscured AGNs, the X-ray radiation is absorbed by gas and dust surrounding the nuclear region and reemitted in the mid- and far-IR after being thermally reprocessed. Since IR radiation is less affected by obscuration than optical and X-ray emission, AGN selection at these wavelengths is less biased against obscured

TABLE 3
X-Ray Properties of X-Ray–selected Compton-thick AGNs

Source Name	$\alpha_{J2000.0}$[b] (deg)	$\delta_{J2000.0}$[b] (deg)	Total Counts (0.3–8 keV)	Flux[a] 0.3–8 keV	0.3–2.5 keV	2.5–8 keV	HR	z_{phot}	N_H^{obsc}	N_H^{restd}	log L[e]
SWIRE J104311.22+591128.2	160.79686	59.191322	12 ± 5	20 ± 8	0 ± 3	38 ± 15	$1.00^{+0.0}_{-0.15}$	2.27	$>30^{+40}_{-23}$	863^{+1151}_{-662}	45.9
SWIRE J104322.07+590648.7	160.84201	59.113667	16 ± 5	25 ± 9	0 ± 3	50 ± 17	$1.00^{+0.0}_{-0.04}$	1.41	$>30^{+\infty}_{-10}$	$312^{+\infty}_{-104}$	45.5
SWIRE J104406.30+583954.1	161.02638	58.665276	22 ± 6	37 ± 11	4 ± 4	63 ± 20	$0.61^{+0.21}_{-0.23}$	2.43[f]	4^{+3}_{-1}	99^{+74}_{-25}	45.7
SWIRE J104407.67+584011.3	161.03212	58.670094	12 ± 5	21 ± 9	0 ± 3	41 ± 17	$1.00^{+0.0}_{-0.13}$	1.42	$>20^{+\infty}_{-11}$	$>200^{+\infty}_{-109}$	45.4
SWIRE J104409.95+585224.8	161.04143	58.873802	11 ± 5	19 ± 8	2 ± 3	33 ± 15	$0.85^{+0.06}_{-0.39}$	2.54[f]	8^{+2}_{-5}	214^{+54}_{-134}	45.6

[a] X-ray flux in 10^{-16} ergs cm^{-2} s^{-1} derived assuming an absorbed power-law model with photon index Γ equal to 1.7 and Galactic N_H (6×10^{19} cm^{-2}). Uncertainties reflect only the statistical errors from the observed counts and do not include uncertainties in the spectral model.
[b] X-ray coordinates.
[c] N_H in the observer rest frame in 10^{22} cm^{-2}.
[d] N_H in the source rest frame in 10^{22} cm^{-2}.
[e] Logarithm of the 0.3–8 keV absorption-corrected rest-frame luminosity in ergs s^{-1}.
[f] Spectroscopic z. Photometric z are reported in Table 4.

AGNs. However, AGNs usually represent only a small fraction of all of the sources detected in IR surveys compared to the far more numerous and strong IR emitters, such as galactic sources and normal and starburst galaxies. Moreover, their IR spectral properties can be indistinguishable from those of non-AGN sources when only a few IR bands are available. IR-selected AGNs can thus be less reliable than X-ray– and optical-selected samples. The *Spitzer Space Telescope* (Werner et al. 2004), thanks to the wavelength range accessible to IRAC (Fazio et al. 2004), offers the capability to easily identify a large fraction of the AGN population (Lacy et al. 2004; Stern et al. 2005) through a simple color analysis that efficiently removes the majority of non-AGN sources.

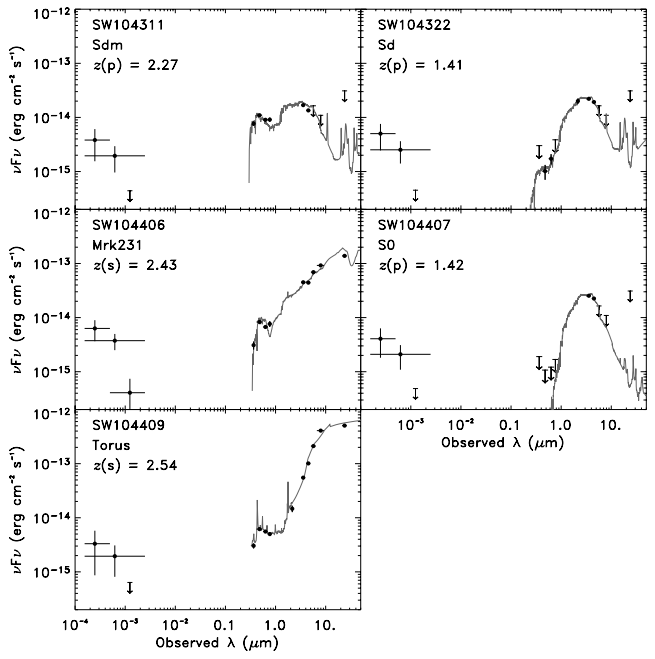

Fig. 1.—SED in $\nu F\nu$ of the five X-ray–selected Compton-thick AGNs (*filled circles*). Abbreviated source names are reported on the upper left corner of each panel. Downward-pointing arrows indicate 5 σ upper limits. The broadband, hard-band, and soft-band X-ray fluxes are shown as crosses. The X-ray flux energy range is indicated by the length of the horizontal line. The X-ray fluxes are derived assuming an absorbed power-law model with photon index Γ equal to 1.7 and Galactic absorption $N_H = 6 \times 10^{19}$ cm^{-2}. A downward-pointing arrow at 2 σ limit is used in the X-rays when the counts are less than 1 σ. The best-fit template for each object is shown as a gray line, and the template name is reported in each panel. The spectroscopic [$z(s)$] or photometric [$z(p)$] redshift of each object is also reported.

In the mid-IR, AGNs are characterized by red and almost featureless spectra (Houck et al. 2005; Hao et al. 2005; Weedman et al. 2005). These properties make their IRAC (3.6, 4.5, 5.8, and 8.0 μm) colors unique among other IR sources, such as galaxies and stars, providing a powerful tool to identify them (Lacy et al. 2004; Stern et al. 2005; Hatziminaoglou et al. 2005). However, this diagnostic is effective only when the AGN is the dominant energy source. In cases where thermal radiation produced by dust associated with the AGN is self-absorbed and/or thermal radiation from dust in star-forming regions is more luminous than that produced by the AGN, e.g., as in the Seyfert 2 galaxies NGC 4945 and NGC 6240 (Maiolino et al. 2003; Rigopoulou et al. 1999), the AGN IR emission is fainter or negligible compared to that produced by star formation processes in the host galaxy (Peeters et al. 2004). The IR SED and IRAC colors of these AGNs may be indistinguishable from those of starburst and normal star-forming galaxies (i.e., dominated by cool/warm dust and polycyclic aromatic hydrocarbon (PAH) features at $z < 0.6$ and by stellar light at $z > 0.6$; Franceschini et al. 2005; Alonso-Herrero et al. 2004; Rigby et al. 2004). In these sources, the AGN might manifest itself at other wavelengths, in the X-rays, if not completely obscured, as in the three stellar-dominated Compton-thick X-ray AGNs reported in § 3.1, in the radio, or in optical and IR spectra, if the light is not diluted by the host galaxy starlight (Moran et al. 2002).

In order to select heavily obscured AGN candidates among the IR population independently of their X-ray properties, we require a red and featureless IR SED and red optical SEDs or red optical–IR colors to remove unobscured AGNs. This requirement would be satisfied by only a subset of all obscured AGNs for the reasons given above. We first selected all of the extragalactic IR sources that are detected at a 5 σ level in at least three IR bands over the wavelength range 3.6–24 μm. This reduced the IR sample from 41,262 to 4493 sources, of which 2726 (60%) are detected at 24 μm. Note that about 46% of the extragalactic X-ray sources with an IR counterpart in the *Chandra*/SWIRE field do not satisfy this selection criterion. The next step in the selection procedure is done automatically through an algorithm that calculates the spectral slope and goodness of a power-law model fit to the observed SED (νF_ν) between 2.15 and 24 μm, which includes the K_s band data, the four IRAC bands, and the MIPS 24 μm band. All of the sources with a monotonically rising IR SED, a spectral slope α_{IR} (defined as $F_\nu \propto \lambda^{\alpha_{IR}}$) larger than 1.0, and reduced $\chi^2_\nu < 13.3(\alpha_{IR} - 1) \leq 20$ are then selected. The slope threshold is defined to reject sources with blue SEDs typical of early-type galaxies. The χ^2 test is used to select sources with smooth red

SEDs, not necessarily power-law like, and to remove sources with variations in their SEDs due to the presence of spectral features, e.g., PAHs. AGNs may show IR SEDs with a convex round shape in $\log F_\nu$ instead of a straight power-law spectrum, or a dip at 24 μm due to the 9.7 μm silicate absorption feature at $z \sim 1.5$ (Franceschini et al. 2005; Alonso-Herrero et al. 2004; Rigby et al. 2004, 2005; Houck et al. 2005; Weedman et al. 2005; Hao et al. 2005). For these AGNs a power-law model fit does not provide a good fit, but it is a reasonable first-order approximation to their IR SEDs. The expected $\alpha_{\rm IR}$ and χ^2_ν values for AGNs and normal galaxies were derived from a simulated catalog of sources of different types and redshifts and several combinations of detections in the same filter systems as available for the SWIRE catalog. The simulated catalog was created from the same template library used to derive photometric redshifts, and uncertainties to the observed fluxes were added in order to resemble those of the SWIRE catalog. The SEDs of a subset of randomly selected objects with a broad range of χ^2 and $\alpha_{\rm IR}$ were also visually inspected for verification and parameter tuning. Nondetections were taken into account by requiring the power-law model to be consistent with the upper limits. This selection reduces the sample from 4493 to 248 sources, of which 93% are detected at 24 μm. Although the selection does not require a detection at 24 μm, the large fraction of 24 μm sources is not surprising due to the combination of the minimum required power-law slope ($\alpha_{\rm IR} = 1$) and the SWIRE sensitivity. The faintest source with $\alpha_{\rm IR} = 1$ and detected in three IRAC bands will have a 24 μm flux of 120 μJy, only a factor of 2 lower than our 5 σ limit. Sources with brighter fluxes and redder SEDs will then be easily detected at 24 μm. Only 23% (90 sources) of the X-ray–detected sources with three IR detections have IR SEDs that satisfy the above criterion. This is consistent with previous SED analyses of X-ray-selected AGNs that find typical AGN SEDs for only ~30% of all X-ray–selected AGNs (Franceschini et al. 2005). In order to remove likely unobscured quasars, we then selected all of the sources with optical–IR colors redder than those typical of unobscured quasars or red optical SEDs. These requirements are satisfied if a power-law ($F_\nu \propto \lambda^{\alpha_{\rm opt}}$) fit to the optical SED of a source detected in g', r', and i' has a slope, $\alpha_{\rm opt}$, greater than 2, or if at least two of the following conditions are verified: $F(3.6\ \mu{\rm m})/F(g') \geq 15$, $F(3.6\ \mu{\rm m})/F(r') \geq 13$, and $F(3.6\ \mu{\rm m})/F(i') \geq 10$. This final criterion is satisfied by 181 sources, of which 78 do not have an optical counterpart at the survey limits (see § 2.1). Note that for blank sources fainter than 16 μJy at 3.6 μm and located where the optical observations are the least sensitive ($\delta < 58.^\circ6$), this criterion cannot be verified, but at this stage of the selection, they are kept in the sample for completeness. This selection removes 67 sources, of which 42 are X-ray sources. Among the rejected sample, 61 sources have optical–IR SEDs consistent with those of unobscured AGNs like optically selected quasars.

The SEDs of the remaining 181 obscured AGN candidates were fitted using HyperZ and the library of 12 normal galaxy and 12 AGN templates. Only the sources that did not have any acceptable solutions (a minimum in the χ^2_ν distribution) with normal galaxy templates were kept, for a final sample of 120 sources. Among the rejected sources, several can be high-redshift galaxies whose optical and near-IR emission is due to stellar light. Some of the rejected sources might host an AGN, but in order to increase our sample reliability, we decided to remove any dubious cases. This selection removes seven X-ray sources from the sample, yielding a total of 41 X-ray sources among the IR-selected obscured AGNs. The X-ray properties of the 41 X-ray sources out of the 120 IR-selected sample of AGN candidates are reported in Table 5 and described in § 3.2.1. For all of the selected sources,

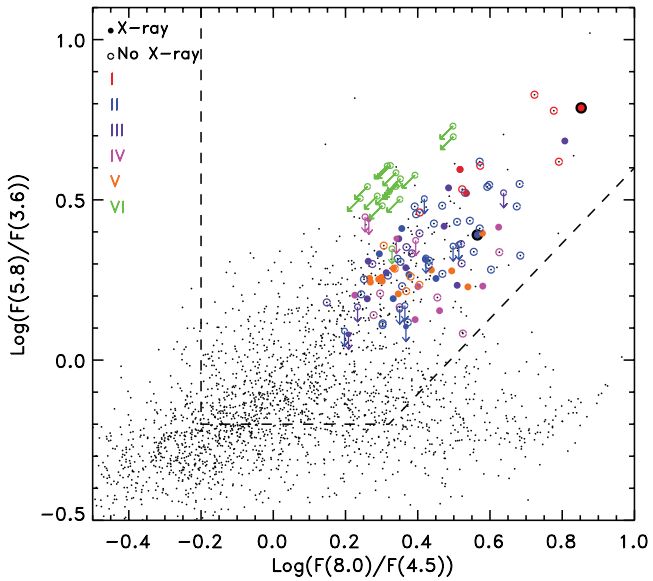

FIG. 2.—IRAC color-color diagram [$F(5.8\ \mu{\rm m})/F(3.6\ \mu{\rm m})$ vs. $F(8.0\ \mu{\rm m})/F(4.5\ \mu{\rm m})$] of all of the IR sources detected in four IRAC bands in the *Chandra*/SWIRE field (*black dots*). IR-selected obscured AGN candidates are shown as open circles, or filled circles if they are also X-ray sources. Downward-pointing arrows indicate sources that are not detected at 5.8 μm, and arrows pointing toward the bottom left corner indicate sources that are not detected at either 5.8 or 8.0 μm. The colors correspond to different SED types (*red*: I; *blue*: II; *purple*: III; *magenta*: IV; *orange*: V; *green*: VI; see § 3.2). The two confirmed Compton-thick quasars, SW 104406 and SW 104409, are shown with large black filled circles (see § 5). The dashed line shows the region preferentially occupied by AGNs, identified by Lacy et al. (2004).

even for those that are not detected in the optical images, the 3.6 μm/optical flux ratio is constrained to be higher than the limits given above. The IRAC colors of the selected sample compared to the rest of the IR sources in the *Chandra*/SWIRE field are shown in Figure 2. The dashed line delimits the region where AGNs are most likely to be found (Lacy et al. 2004; see also Stern et al. 2005; Hatziminaoglou et al. 2005).

In the initial sample of 4493 sources, less than 9% are X-ray sources, but 34% of the selected sample of obscured AGN candidates are X-ray sources. Among the IR-selected AGNs that were rejected because they are consistent with unobscured AGNs, 63% are X-ray sources. These values are consistent with a selection that favors AGNs. Only two sources are not detected at 24 μm, and four have a 24 μm flux below the nominal 5 σ limit. A 24 μm detection for these four sources was confirmed after a visual inspection of the images. Note that the sensitivity of the 24 μm data varies across the field due to a variation in the number of coverages. The adopted 5 σ limit of 230 μJy is valid for the areas with median coverage in the *Chandra*/SWIRE field.

The sample was divided into six categories, from I to VI; five categories (I–V) were defined based on their best-fit template, while one category (VI) was defined based on the low number (three) of detections in the IR. Class I sources (nine) have IR SEDs characterized by a convex shape that are well fitted with a "torus" template (see § 5.1). Class II sources (44) show power-law–like optical–IR SEDs, similar to Mrk 231 or slightly redder ($A_V < 1$). Similarly, class III sources (19) have power-law–like optical–IR SEDs, but not as red as Mrk 231; a reddened QSO template ($A_V = 0.6-1.0$) provides a better fit. Class IV sources (16) show SEDs consistent with templates of composite sources with contributions from both star-forming regions and an AGN component. This interpretation is supported by an excess at

TABLE 4
PROPERTIES OF IR-SELECTED OBSCURED AGN CANDIDATES

Source Name	α[a] (deg)	δ[a] (deg)	mag (r') (Vega)	$F_{3.6\,\mu m}$ (μJy)	$F_{4.5\,\mu m}$ (μJy)	$F_{5.8\,\mu m}$ (μJy)	$F_{8.0\,\mu m}$ (μJy)	$F_{24\,\mu m}$ (μJy)	$F_{20\,cm}$ (μJy)	z_{spec}	z_{phot}	Class[b]
SWIRE J104314.93+585606.3	160.81221	58.935070	>24.4	9	22	63	116	936	90 ± 23	...	3.07	I
SWIRE J104409.95+585224.8	161.04146	58.873550	23.55	65	152	401	1082	4011	273 ± 15	2.540	2.67	I[c]
SWIRE J104531.45+591027.0	161.38103	59.174160	>25.2	28	54	110	179	1189	103 ± 5	...	1.97	I[c]
SWIRE J104605.11+584310.8	161.52130	58.719662	>25.2	14	26	59	162	707	58 ± 11	...	2.03	I
SWIRE J104605.54+583742.5	161.52309	58.628460	>24.4	12	21	72	127	1359	<91	...	3.63	I
SWIRE J104633.45+590016.7	161.63937	59.004631	>25.2	17	35	67	131	355	33 ± 3	...	1.50	I
SWIRE J104659.42+584624.1	161.74757	58.773350	>25.2	27	50	77	128	538	223 ± 16	...	1.18	I
SWIRE J104811.23+592206.8	162.04680	59.368561	>24.4	53	96	181	319	1315	<198	...	1.32	I
SWIRE J104825.76+591338.9	162.10732	59.227470	>24.4	45	70	150	241	1234	154 ± 23	...	1.31	I[c]

NOTES.—Typical uncertainties to the IR fluxes are ~10% of the measured fluxes and to the optical magnitudes are around 0.04 mag. Upper limits correspond to 5 σ values. Table 4 is published in its entirety in the electronic edition of the *Astrophysical Journal*. A portion is shown here for guidance regarding its form and content.

[a] IR coordinates.

[b] Class I sources are characterized by convex IR SEDs fitted by a "torus" template. Class II sources show power-law–like optical–IR SEDs, similar to Mrk 231 or slightly redder ($A_V < 1$). Class III sources have power-law–like optical–IR SEDs fitted by a reddened QSO template ($A_V = 0.6-1.0$). Class IV sources show signatures from both a starburst and an AGN component. Class V sources are characterized by very red optical SEDs and power-law–like IR SEDs. Class VI objects are detected only in three bands from 3.6 to 24 μm.

[c] X-ray source.

24 μm with respect to the extrapolation of the power law representing the hot dust continuum associated with the AGN; this excess is likely associated with emission from the PAH bands. Class V objects (16) are characterized by a turnover in the SED with optical SEDs much redder than the IR SED. These sources might be composite objects where the optical emission is dominated by stellar light, from either an old or a reddened stellar population, and the IR emission is associated with the AGN. Class VI objects (16) are fainter than the rest of the sample and detected only in three bands from 3.6 to 24 μm; their SEDs show a distinct signature of AGNs in their extreme red $F(4.5\ \mu m)/F(3.6\ \mu m)$ flux ratios. Upper limits to the flux in the bands are consistent with the models used to describe the other classes. Names, coordinates, r' magnitudes, IR fluxes, and classification of the IR-selected obscured AGN candidates are listed in Table 4, and their SEDs are shown in Figure 3. Photometric redshifts were used to overplot the best-fit template on each SED when spectroscopic redshifts were not available. The redshifts are used only to visually characterize the SED shape of these sources by comparing them with AGN templates.

Only 11 sources have spectroscopic redshifts. Spectroscopic redshifts are indicated as $z(s)$ and photometric redshifts as $z(p)$ in Figure 3 and listed in Table 4. The optical spectra of seven sources (SW 104351, $z = 0.609$; SW 104409, $z = 2.540$; SW 104406, $z = 2.430$; SW 104447, $z = 2.488$; SW 104644, $z = 2.542$; SW 104657, $z = 1.579$; and SW 104700, $z = 2.562$) show emission lines from an AGN (e.g., Lyα, C IV λ1549), and their width ranges from 1200 to ~1700 km s^{-1}, typical of narrow-line or type 2 AGNs. The optical spectrum of SW 104407 ($z = 0.555$) is dominated by stellar light typical of a poststarburst galaxy (Balmer absorption line) and high-ionization narrow emission lines ([Ne V] λ3426, [Ne III] λ3869) from the AGN. Two sources, SW 104353 ($z = 0.563$) and SW 104458 ($z = 1.52$), show only one emission line, [O II] λ3727, consistent with emission from newborn stars. No AGN signatures are observed, but the optical spectra are characterized by low signal-to-noise ratio. The spectrum of SW 104504 ($z = 0.214$) shows broad Balmer emission lines, Hα, Hβ, and the [O III] λ5007 forbidden line, typical of a starburst galaxy.

3.2.1. *X-Ray Properties of the IR-selected Obscured AGN Candidates*

A total of 41 sources, corresponding to 34% of the IR-selected obscured AGN candidates, are also X-ray detected. Five of these 41 X-ray sources have multiple IR counterparts. However, in all five cases the matched source is at less than 1″ from the X-ray source with a probability of random association <1.3%, and the neighbor sources are more than 2″ distant. Therefore, we consider all these associations reliable. The 41 X-ray sources show all types of optical–IR SEDs, except class VI. Their X-ray spectra (see Table 5) show a wide range of HRs, from −0.87 to 0.90, with a median value of −0.26. Assuming our redshift estimates to derive the intrinsic column density and a photon index $\Gamma = 1.7$, 26 (63%) sources have column densities larger than 10^{22} cm^{-2}, and of these, 12 have $N_H > 10^{23}$ cm^{-2}. Only two sources are also present in the X-ray–selected sample of Compton-thick ($N_H > 10^{24}$ cm^{-2}) AGNs, SWIRE J104409.95+585224.8 (hereafter SW 104409) and SWIRE J104406.30+583954.1 (hereafter SW 104406).

3.2.2. *Optical versus X-Ray Flux*

The optical and broadband (0.3–8 keV) X-ray fluxes of all of the X-ray sources in the *Chandra*/SWIRE field and of the IR-selected obscured AGN candidates are compared in the top panel of Figure 4, where the X-ray sample is shown as black open circles and the IR-selected sample as filled circles. We use the full-band flux to minimize the uncertainty associated with the factors used to convert counts to flux. The distribution of r'-band fluxes for the IR-selected sample is shown in the bottom panel of Figure 4. The sample of IR-selected obscured AGN candidates is shown as filled circles of different colors according to their classification (*red*: I; *blue*: II; *purple*: III; *magenta*: IV; *orange*: V; *green*: VI). The X-ray–selected sources are shown as cyan filled circles. In the case of no optical detection a left-pointing arrow at the 5 σ r'-band value is shown, and in the case of no X-ray detection a downward-pointing arrow at 10^{-15} ergs cm^{-2} s^{-1} is shown. We also plot the expected observed fluxes of four AGN templates at various redshifts from 0.1 to 3. The AGN templates correspond to the median of a sample of optically selected quasars (Elvis et al. 1994): the "Elvis QSO," the Compton-thick broad absorption line (BAL) QSO/Seyfert 1 galaxy Mrk 231 ($z = 0.042$; Braito et al. 2004), and the Compton-thick Seyfert 2 galaxies IRAS 19254−7245 South ($z = 0.0617$; Berta et al. 2003; Braito et al. 2003) and NGC 6240 ($z = 0.0244$; Vignati et al. 1999; Iwasawa et al. 2001). All templates other than the Elvis QSO are characterized by extreme (Compton-thick) absorption in the X-rays. The hatched area represents the locus of

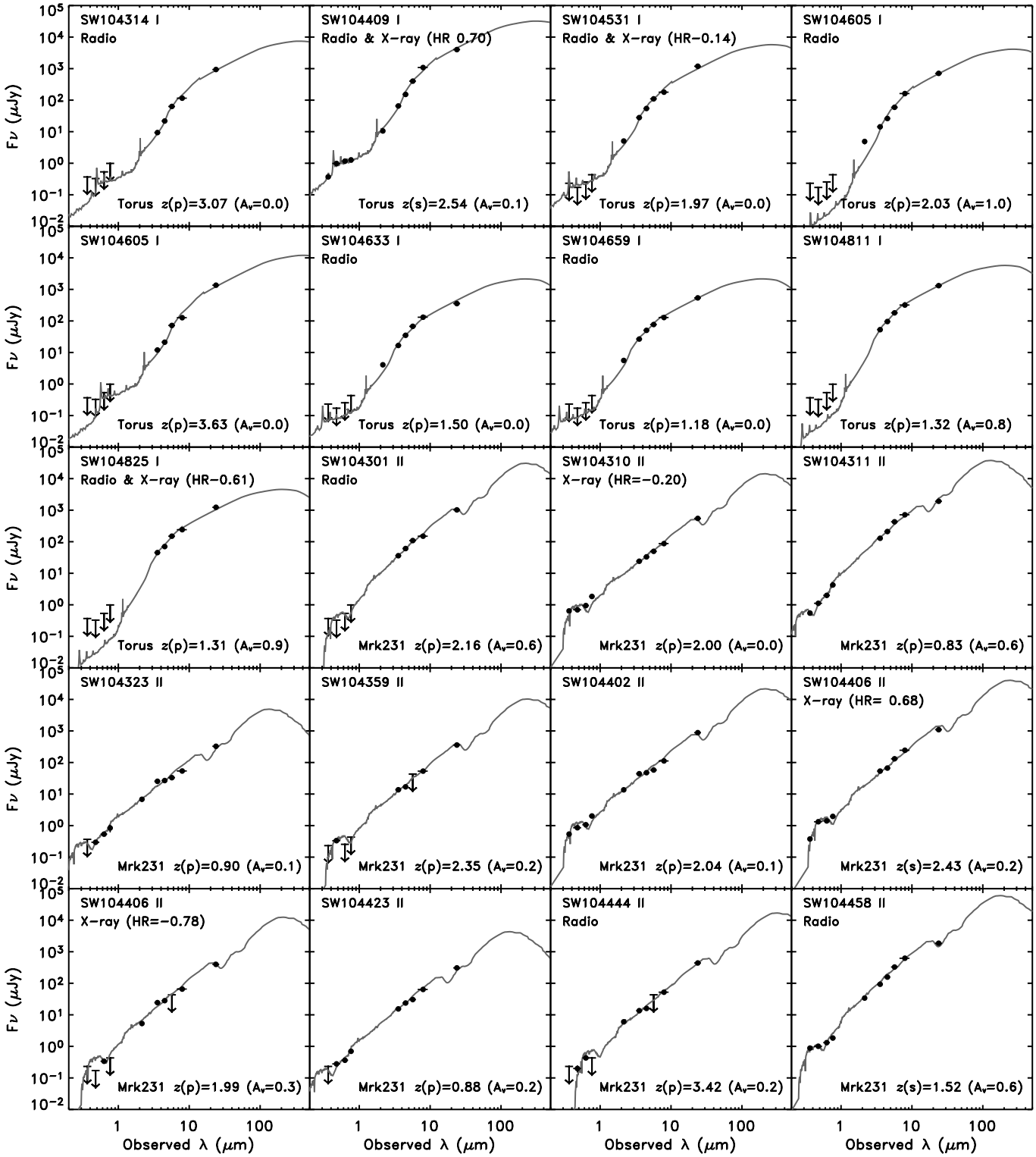

FIG. 3.—SEDs of the 120 IR-selected obscured AGN candidates. The 5 σ upper limits are reported as downward-pointing arrows. The sources are ordered by SED class, from I to VI (see text) and by right ascension within each SED class. The abbreviated source name and the SED class are given on the upper left corner of each panel. Each SED class is fitted with an AGN template (I: torus; II: Mrk 231; III: QSO 1; IV: IRAS 19254−7245 South; V: QSO 2; VI: any of the previous templates). The best-fit template for each source at the spectroscopic redshift, $z(s)$, if available, or at the photometric redshift, $z(p)$, is shown as a gray line. The amount of extinction applied to the template and the redshift are reported on the bottom right corner in each panel. X-ray sources are identified by the note "X-ray" on the upper left corner and the HR value is also given, and radio sources are identified by the note "Radio." [*See the electronic edition of the Journal for panels b–f of this figure*.]

TABLE 5

X-RAY PROPERTIES OF IR-SELECTED AGNS

Source Name	Total Counts (0.3–8 keV)	$F_{0.3-8\,\mathrm{keV}}$[a] (10^{-16} ergs cm^{-2} s^{-1})	$F_{0.3-2.5\,\mathrm{keV}}$[a] ($10^{-16}$ ergs cm^{-2} s^{-1})	$F_{2.5-8\,\mathrm{keV}}$[a] (10^{-16} ergs cm^{-2} s^{-1})	HR	z	$N_{\mathrm{H}}^{\mathrm{obs}}$[b] ($10^{22}$ cm^{-2})	$N_{\mathrm{H}}^{\mathrm{rest}}$[c] ($10^{22}$ cm^{-2})	log L[d]	Class
SWIRE J104409.95+585224.8	11 ± 5	19 ± 8	2 ± 3	33 ± 15	$0.85^{+0.06}_{-0.39}$	2.540[e]	8.0	214.0	45.637	I
SWIRE J104531.45+591027.0	7 ± 4	12 ± 7	5 ± 4	10 ± 11	$-0.14^{+0.76}_{-0.84}$	1.973	0.7	11.6	43.986	I
SWIRE J104825.76+591338.9	21 ± 7	34 ± 12	19 ± 7	13 ± 16	$-0.61^{+0.45}_{-0.00}$	1.307	<0.1	0.1	43.497	I
SWIRE J104310.29+585916.0	118 ± 13	202 ± 22	84 ± 12	162 ± 30	$-0.20^{+0.20}_{-0.20}$	1.997	0.6	10.0	45.186	II
SWIRE J104406.30+583954.1	22 ± 6	37 ± 11	4 ± 4	63 ± 20	$0.61^{+0.21}_{-0.23}$	2.430[e]	4.3	99.0	45.738	II
SWIRE J104406.71+585130.8	10 ± 5	17 ± 8	10 ± 5	4 ± 10	$-0.78^{+0.38}_{-0.33}$	1.991	<0.1	0.2	43.645	II
SWIRE J104525.21+585949.3	16 ± 5	27 ± 9	15 ± 6	10 ± 12	$-0.62^{+0.34}_{-0.18}$	2.045	<0.1	0.2	43.882	II
SWIRE J104551.81+590345.3	10 ± 5	17 ± 8	5 ± 4	19 ± 13	$0.10^{+0.56}_{-0.65}$	0.999	1.3	7.8	43.363	II
SWIRE J104633.29+584820.3	6 ± 4	10 ± 7	5 ± 4	6 ± 10	$-0.40^{+0.87}_{-0.00}$	2.693	0.2	6.4	44.102	II
SWIRE J104735.93+590549.7	34 ± 7	55 ± 11	21 ± 6	48 ± 16	$-0.12^{+0.20}_{-0.19}$	1.644	0.8	9.4	44.412	II
SWIRE J104836.72+585414.7	59 ± 9	98 ± 15	54 ± 9	39 ± 16	$-0.60^{+0.13}_{-0.11}$	0.533	<0.1	<0.1	43.002	II
SWIRE J104903.66+590006.9	19 ± 7	32 ± 12	21 ± 7	4 ± 16	$-0.87^{+0.38}_{-0.00}$	1.641	<0.1	0.1	43.716	II
SWIRE J104321.34+590943.0	1227 ± 36	1980 ± 58	993 ± 34	1092 ± 63	$-0.45^{+0.02}_{-0.03}$	2.294	0.1	2.9	46.108	III
SWIRE J104353.42+585316.2	49 ± 8	84 ± 14	25 ± 7	95 ± 22	$0.14^{+0.16}_{-0.16}$	0.563[e]	1.4	4.5	43.380	III
SWIRE J104432.03+590457.7	134 ± 14	230 ± 23	83 ± 12	221 ± 34	$-0.04^{+0.18}_{-0.18}$	0.896	0.9	4.9	44.308	III
SWIRE J104500.71+591353.4	16 ± 5	29 ± 9	9 ± 5	32 ± 15	$0.11^{+0.30}_{-0.30}$	0.700	1.3	5.3	43.161	III
SWIRE J104616.93+585457.1	49 ± 8	84 ± 15	37 ± 8	62 ± 19	$-0.27^{+0.26}_{-0.22}$	0.705	0.4	1.8	43.494	III
SWIRE J104641.38+585213.9	12 ± 5	19 ± 8	9 ± 5	14 ± 12	$-0.26^{+0.48}_{-0.49}$	1.095	0.4	3.1	43.367	III
SWIRE J104644.18+590027.8	33 ± 7	56 ± 12	23 ± 7	46 ± 17	$-0.19^{+0.26}_{-0.24}$	2.542[e]	0.6	15.7	44.976	III
SWIRE J104749.61+584845.7	45 ± 8	75 ± 14	39 ± 8	37 ± 16	$-0.50^{+0.24}_{-0.20}$	0.695	0.05	0.2	43.237	III
SWIRE J104826.99+585438.8	16 ± 5	27 ± 9	8 ± 5	30 ± 14	$0.10^{+0.28}_{-0.31}$	1.410	1.3	12.8	44.019	III
SWIRE J104913.37+585946.3	39 ± 9	65 ± 15	21 ± 7	70 ± 23	$0.07^{+0.26}_{-0.18}$	3.435	1.2	58.8	45.861	III
SWIRE J104241.45+591357.2	28 ± 7	45 ± 12	23 ± 7	22 ± 15	$-0.51^{+0.26}_{-0.22}$	1.434	0.04	0.4	43.812	IV
SWIRE J104254.46+591013.3	32 ± 7	52 ± 11	18 ± 6	53 ± 17	$0.03^{+0.21}_{-0.21}$	1.541	1.1	12.3	44.385	IV
SWIRE J104420.22+583948.0	56 ± 9	97 ± 15	30 ± 7	107 ± 23	$0.11^{+0.16}_{-0.16}$	1.700	1.3	17.5	44.842	IV
SWIRE J104528.29+591326.7	18 ± 5	31 ± 10	9 ± 5	35 ± 15	$0.16^{+0.27}_{-0.28}$	0.669	1.5	5.5	43.153	IV
SWIRE J104733.46+592108.1	40 ± 8	70 ± 13	40 ± 8	24 ± 14	$-0.65^{+0.15}_{-0.12}$	1.107	<0.1	0.1	43.628	IV
SWIRE J104736.92+591941.3	9 ± 4	15 ± 8	9 ± 5	6 ± 10	$-0.60^{+0.63}_{-0.00}$	1.543	<0.1	0.1	43.332	IV
SWIRE J104754.78+590810.4	16 ± 5	25 ± 9	14 ± 5	11 ± 11	$-0.57^{+0.28}_{-0.24}$	1.826	<0.1	0.1	43.728	IV
SWIRE J104813.49+590340.7	17 ± 5	28 ± 9	17 ± 6	6 ± 10	$-0.79^{+0.21}_{-0.14}$	1.818	<0.1	0.1	43.769	IV
SWIRE J104303.50+585718.1	14 ± 7	24 ± 11	3 ± 5	38 ± 19	$0.60^{+0.62}_{-0.70}$	0.595	3.6	12.0	43.073	V
SWIRE J104351.87+584953.7	44 ± 8	75 ± 14	10 ± 5	121 ± 25	$0.61^{+0.25}_{-0.31}$	0.609[e]	3.6	12.5	43.605	V
SWIRE J104407.97+584437.0	48 ± 8	83 ± 14	30 ± 8	81 ± 21	$-0.03^{+0.20}_{-0.20}$	0.555[e]	1.0	3.0	43.306	V
SWIRE J104422.64+591304.1	800 ± 29	1292 ± 48	649 ± 28	711 ± 52	$-0.45^{+0.09}_{-0.08}$	0.323	0.1	0.3	43.730	V
SWIRE J104503.56+585109.9	29 ± 8	49 ± 14	18 ± 7	45 ± 20	$-0.08^{+0.29}_{-0.28}$	0.981	0.8	4.9	43.729	V
SWIRE J104504.96+585947.3	59 ± 9	102 ± 16	3 ± 5	193 ± 31	$0.90^{+0.06}_{-0.14}$	0.214[e]	8.7	14.3	42.736	V
SWIRE J104532.93+584638.6	101 ± 12	176 ± 20	98 ± 12	69 ± 22	$-0.60^{+0.18}_{-0.15}$	1.781	<0.1	0.1	44.545	V
SWIRE J104725.94+591025.5	136 ± 13	219 ± 21	116 ± 13	102 ± 23	$-0.54^{+0.10}_{-0.10}$	0.668	<0.1	<0.1	43.585	V
SWIRE J104731.84+592432.9	31 ± 7	55 ± 12	24 ± 7	40 ± 17	$-0.28^{+0.24}_{-0.22}$	3.108	0.4	16.6	45.174	V
SWIRE J104748.27+590534.7	15 ± 5	24 ± 9	12 ± 5	14 ± 12	$-0.43^{+0.38}_{-0.32}$	1.041	0.2	1.1	43.292	V
SWIRE J104829.49+591249.1	67 ± 10	108 ± 16	50 ± 9	72 ± 21	$-0.33^{+0.24}_{-0.22}$	0.280	0.3	0.6	42.577	V

[a] X-ray flux derived assuming an absorbed power-law model with photon index Γ equal to 1.7 and Galactic N_{H} (6×10^{19} cm^{-2}). Uncertainties reflect only the statistical errors from the observed counts and do not include uncertainties in the spectral model.

[b] N_{H} in the observer rest frame.

[c] N_{H} in the source rest frame.

[d] Logarithm of the 0.3–8 keV absorption-corrected rest-frame luminosity in ergs s^{-1}.

[e] Spectroscopic z. Photometric z are reported in Table 4.

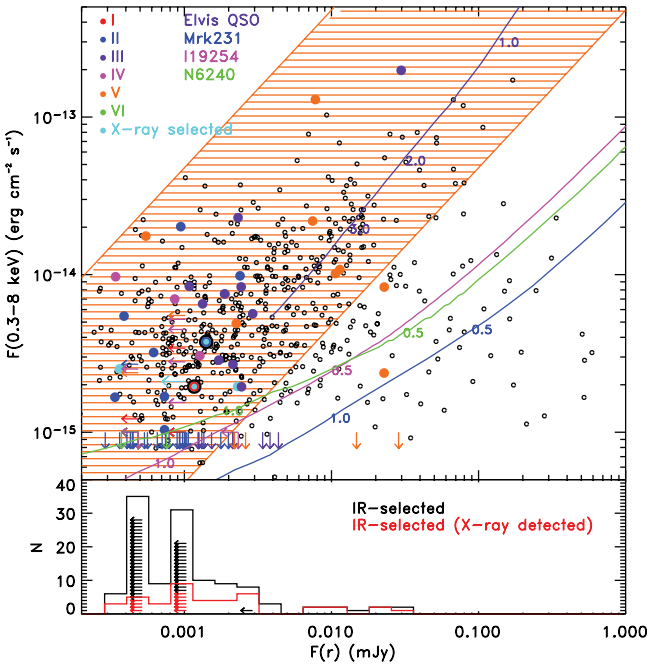

FIG. 4.—*Top*: Broad (0.3–8 keV) X-ray flux vs. the r'-band flux of all of the X-ray sources in the *Chandra*/SWIRE field (*black open symbols*), of X-ray–selected obscured AGN candidates (*cyan*), and of IR-selected obscured AGN candidates (*red*: I; *blue*: II; *purple*: III; *magenta*: IV; *orange*: V; *green*: VI). Downward-pointing arrows represent sources not detected in the X-rays, and leftward-pointing arrows represent sources not detected in the optical r' band. The X-ray fluxes are derived assuming an absorbed power-law model with photon index Γ equal to 1.7 and Galactic absorption $N_{\rm H} = 6 \times 10^{19}$ cm^{-2}. The two Compton-thick quasars, SW 104406 and SW 104409, are shown with large black filled circles. The orange hatched area delimits the region of $\log [F(\rm X)/\nu F(r')] = \pm 1$, typical of classical AGNs. The purple, blue, magenta, and green lines represent the tracks of known AGNs at various redshifts as annotated, the Elvis QSO template (*purple*), Mrk 231 (*blue*), IRAS 19254−7245 South (*magenta*), and NGC 6240 (*green*). *Bottom*: Distribution of the r'-band flux of the IR-selected sample of obscured AGN candidates. The black line represents the entire IR-selected sample; the red line shows only the X-ray–detected subsample. Left-pointing arrows represent r'-band 5 σ upper limits; each arrows refers to a single source.

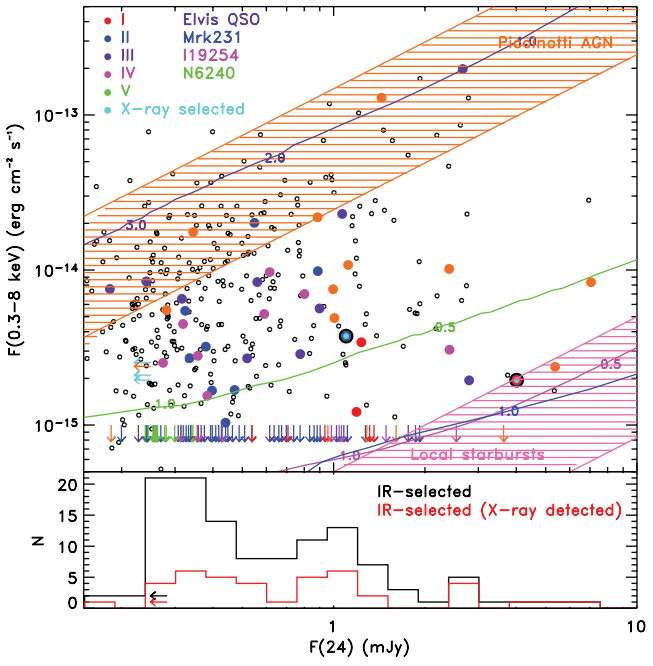

FIG. 5.—*Top*: Broad (0.3–8 keV) X-ray flux vs. the 24 μm flux of all of the X-ray sources in the *Chandra*/SWIRE field (*black open circles*). Symbols as in Fig. 4. The orange hatched area represents the area that the AGN in the Piccinotti sample (Piccinotti et al. 1982) would occupy, and the pink hatched area represents the area that the local starburst galaxy would occupy (adopted from Alonso-Herrero et al. 2004). The X-ray fluxes are derived assuming an absorbed power-law model with photon index Γ equal to 1.7 and Galactic absorption $N_{\rm H} = 6 \times 10^{19}$ cm^{-2}. *Bottom*: Distribution of the 24 μm flux of the IR-selected sample of obscured AGN candidates. The black line represents the entire IR-selected sample; the red line refers only to the X-ray–detected subsample. Left-pointing arrows represent 24 μm 5 σ upper limits.

$F(\rm X)/\nu F(r')$ between 0.1 and 10, which is traditionally considered the locus where "classical" AGNs lie (Akiyama et al. 2003). Sources with $F(\rm X)/\nu F(r') > 10$ are expected to be mostly obscured AGNs at high z (Perola et al. 2004), while sources with $F(\rm X)/\nu F(r') < 0.1$ are expected to be mostly star-forming galaxies whose X-ray emission is not powered by an AGN. However, this simple picture becomes more complex for fainter AGNs (Comastri et al. 2003).

The three Compton-thick AGN templates are characterized by low X-ray/optical flux ratios $[F(\rm X)/\nu F(r') < 0.1]$ at low z, and as the redshift increases, they move into the locus of "classical" AGNs. Thus, extreme $F(\rm X)/\nu F(r')$ ratios are not expected for local Compton-thick AGNs even at high redshifts. Lower flux ratios $[F(\rm X)/\nu F(r') = 0.1-10]$, consistent with those of classical AGNs, are also observed in the X-ray–selected Compton-thick AGN sample. The majority (108) of the IR-selected obscured AGN candidates also have $F(\rm X)/\nu F(r') = 0.1-10$, 91 of which show $F(\rm X)/\nu F(r')$ between 0.1 and 1, and 12 sources have $F(\rm X)/\nu F(r') < 0.1$. It is clear that obscured AGNs do not have unique $F(\rm X)/\nu F(r')$ ratios. Therefore, a selection based on large (>10) $F(\rm X)/\nu F(r')$ values would miss a large fraction of obscured AGNs.

3.2.3. *Mid-Infrared versus X-Ray Flux*

The observed mid-IR flux at 24 μm and the broadband (0.3–8 keV) X-ray flux for the X-ray sample in the *Chandra*/SWIRE field are compared in the top panel of Figure 5, where the X-ray sample is shown as black open circles. Downward-pointing arrows indicate the full-band (0.3–8 keV) flux upper limit of 1×10^{-15} ergs cm^{-2} s^{-1}, and leftward-pointing arrows indicate the 230 μJy 5 σ limit at 24 μm. The sample of X-ray– and IR-selected obscured AGNs shown in Figure 4 is also shown in Figure 5 as filled circles or downward-pointing arrows in colors corresponding to different classes (from I to VI). The lines represent the expected observed fluxes of the four AGN templates shown in Figure 4 at various redshifts from 0.1 to 3. In the bottom panel of Figure 5, the distribution of 24 μm fluxes of the IR-selected sample of obscured AGN candidates is shown.

Hard X-ray–mid-IR flux ratios in the local universe range from 10^{-3} for starburst galaxies to $\simeq$1 for unobscured AGNs (Alexander et al. 2001; Manners et al. 2004; Lutz et al. 2004). The locus occupied by hard X-ray–selected AGNs from the Piccinotti et al. (1982) sample with detected mid-IR emission and $z < 0.12$ corresponds to the hatched area in orange $[F(\rm X)/\nu_{24} F(24\ \mu\rm m) = 0.19-1.17]$. The locus occupied by local starburst galaxies corresponds to the hatched pink area $[F(\rm X)/\nu_{24} F(24\ \mu\rm m) = 5 \times 10^{-4}$ to $3 \times 10^{-3}]$. The two loci have been adapted from Alonso-Herrero et al. (2004) after correcting the X-ray flux from 2–10 keV to 0.3–8 keV assuming an absorbed power-law model with $N_{\rm H} = 10^{21}$ cm^{-2} and spectral index $\Gamma = 1.7$ for the Piccinotti sample and $\Gamma = 2.0$ for the starbursts. Sources with low or no absorption, such as the Elvis QSO template, show large X-ray/mid-IR flux ratios that are almost constant up to $z = 4$ (0.6–0.9). Sources characterized by large column densities are characterized by a broader range of $F(\rm X)/\nu_{24} F(24\ \mu\rm m)$ values, from 6×10^{-4} to 0.6 for $z < 4$. Their X-ray/mid-IR flux

TABLE 6
PHOTOMETRIC DATA FOR SW 104409

Observed Bandpass	Rest-Frame Bandpass	Magnitude (Vega)	Flux Density (ergs cm^{-2} s^{-1} μJy^{-1})	Instrument
0.3–2.5 keV	1.1–8.8 keV	...	$(2 \pm 3) \times 10^{-16}$	*Chandra*/ACIS
2.5–8.0 keV	8.8–28.3 keV	...	$(33 \pm 15) \times 10^{-16}$	*Chandra*/ACIS
0.3–8.0 keV	1.1–28.3 keV	...	$(19 \pm 8) \times 10^{-16}$	*Chandra*/ACIS
U 3647 Å	1031 Å	24.29 ± 0.10	0.369 ± 0.033	KPNO/Mosaic
g' 4782 Å	1351 Å	24.00 ± 0.07	0.983 ± 0.060	KPNO/Mosaic
r' 6288 Å	1777 Å	23.55 ± 0.04	1.166 ± 0.040	KPNO/Mosaic
i' 7665 Å	2166 Å	23.22 ± 0.07	1.279 ± 0.071	KPNO/Mosaic
K_s 2.153 μm	6085 Å	19.37 ± 0.14	10.55 ± 1.42	Palomar/WIRC
3.6 μm	1.01 μm	...	65.5 ± 0.9	*Spitzer*/IRAC
4.5 μm	1.27 μm	...	152 ± 2	*Spitzer*/IRAC
5.8 μm	1.61 μm	...	401 ± 5	*Spitzer*/IRAC
8.0 μm	2.25 μm	...	1082 ± 6	*Spitzer*/IRAC
24. μm	6.74 μm	...	4011 ± 20	*Spitzer*/MIPS
1.4 GHz	4.95 GHz	...	273 ± 15	VLA

ratios increase at larger redshifts, moving them into the region occupied by unobscured AGNs. As absorption increases, the X-ray flux decreases, while the 24 μm flux is only slightly affected. At higher z, however, the IR flux decreases more rapidly since the observed wavelengths correspond to shorter wavelengths in the rest frame and the X-ray flux becomes less affected by obscuration as higher energy photons are collected, resulting in larger X-ray/24 μm flux ratios (Alexander et al. 2001; Fadda et al. 2002; Manners et al. 2004).

All of the X-ray–selected Compton-thick AGNs show X-ray/mid-IR flux ratios lower than those of unobscured AGNs [$F(X)/\nu_{24}F(24\ \mu m) = 0.001-0.03$]. Among the IR-selected obscured AGN candidates, only seven sources (SW 104310, SW 104321, SW 104422, SW 104532, SW 104616, SW 104725, SW 104749) have $F(X)/\nu_{24}F(24\ \mu m) > 0.19$ as in the Piccinotti sample. Three of these seven sources are obscured in the X-rays ($N_H > 10^{22}$ cm^{-2}). Thus, obscured AGNs do not show unique $F(X)/\nu_{24}F(24\ \mu m)$ values; however, low values (<0.2) are more likely. This result is in agreement with a recent study of X-ray– and 24 μm–selected AGNs, which shows that there is no correlation between $F(X)/\nu_{24}F(24\ \mu m)$ and the amount of absorption in the X-ray or optical properties (Rigby et al. 2005).

The ranges of IR and optical fluxes of the X-ray–detected sources are very similar to the values observed in the entire IR-selected sample of obscured AGN candidates (see bottom panels of Figs. 4 and 5). However, there is a higher fraction of faint sources in the whole sample compared to the X-ray–detected subsample, and the majority of sources have smaller X-ray/24 μm flux ratios. Smaller ratios suggest that the fraction of obscured sources and/or the amount of absorption are higher in the non–X-ray-detected subsample. Since we cannot quantify the amount of obscuration in the non–X-ray-detected sources, we assume that the distribution of absorption in the entire IR-selected sample is similar to that observed in the X-ray–detected subsample (63% with $N_H > 10^{22}$ cm^{-2}, 29% with $N_H > 10^{23}$ cm^{-2}, and 5% with $N_H > 10^{24}$ cm^{-2}). However, it is plausible that the estimated fractions of obscured sources are only lower limits to the real distribution for the reasons given above.

Although the ratios between the X-ray flux and the optical or the mid-IR flux are affected by absorption, they cannot be used as an effective method to select obscured AGNs. As shown in the two previous sections and in previous works (Rigby et al. 2004), these flux ratios also depend on the AGN luminosity, the host galaxy contribution, and redshift; therefore, they are not unique for AGNs with large amounts of absorption.

3.2.4. *Radio Properties of the IR-selected Obscured AGN Candidates*

Although a detailed discussion on the radio properties of the AGNs in this field and on the radio population in general will be presented in future works, here we give a brief summary of the radio detection rate of the IR-selected obscured AGN candidates. Half (60 sources) of the sample is detected in the radio (see Table 4). The fraction of radio sources per class I, II, III, IV, V, and VI is, respectively, 77%, 50%, 57%, 43%, 56%, and 25%. The fraction of radio sources among the IR-selected obscured AGN candidates is much higher than the fraction of radio sources among either all IR sources or all X-ray sources. More specifically, within 12′ from the center of the radio field, there are 26 IR-selected obscured AGNs and 24 (=92%) radio sources. The fraction of radio sources in this area per class is 100% (2/2) of class I, 92% (11/12) of class II, 100% (6/6) of class III, 100% (1/1) of class IV, 75% (3/4) of class V, and 100% (1/1) of class V. Since large ratio powers are usually associated with the presence of an AGN, the high fraction of radio detection of this sample is consistent with the hypothesis that these sources are mainly powered by an AGN.

4. PHOTOMETRIC AND SPECTROSCOPIC DATA OF SW 104409 AND SW 104406

Having discussed some general properties of the X-ray– and IR-selected obscured AGN candidates in the *Chandra*/SWIRE field, we now focus on the only two sources that are selected by both selection methods, SW 104409 and SW 104406. These two sources are the only ones among the X-ray sample of Compton-thick AGNs for which a spectroscopic redshift is available, providing a confirmation of their Compton-thick nature. In this section we review the available multiwavelength data for the two sources, and in the next section we construct their SEDs, compare them to those of other Compton-thick AGNs, and present a simple model to explain the observed properties.

Optical and IR photometric fluxes as measured during the observations described in § 2.1 for SW 104409 and SW 104406 are listed in Tables 6 and 7, respectively.

4.1. *Optical Spectroscopy*

Spectroscopic observations for SW 104409 and SW 104406 were carried out on 2005 March 3 and 4, respectively, with the

TABLE 7
PHOTOMETRIC DATA FOR SW 104406

Observed Bandpass	Rest-Frame Bandpass	Magnitude (Vega)	Flux Density (ergs cm^{-2} s^{-1} μJy^{-1})	Instrument
0.3–2.5 keV	1.03–8.6 keV	...	$(4 \pm 4) \times 10^{-16}$	*Chandra*/ACIS
2.5–8.0 keV	8.6–27.4 keV	...	$(63 \pm 20) \times 10^{-16}$	*Chandra*/ACIS
0.3–8.0 keV	1.03–27.4 keV	...	$(37 \pm 11) \times 10^{-16}$	*Chandra*/ACIS
U 3647 Å	1063 Å	24.27 ± 0.17	0.376 ± 0.033	KPNO/Mosaic
g' 4782 Å	1394 Å	23.68 ± 0.05	1.323 ± 0.060	KPNO/Mosaic
r' 6288 Å	1833 Å	23.35 ± 0.06	1.407 ± 0.040	KPNO/Mosaic
i' 7665 Å	2235 Å	22.76 ± 0.13	1.954 ± 0.071	KPNO/Mosaic
K_s 2.153 μm	6278 Å	18.59 ± 0.17	24.52 ± 3.25	Palomar/WIRC
3.6 μm	1.04 μm	...	53.4 ± 1.3	*Spitzer*/IRAC
4.5 μm	1.31 μm	...	67.6 ± 1.2	*Spitzer*/IRAC
5.8 μm	1.66 μm	...	131 ± 7	*Spitzer*/IRAC
8.0 μm	2.32 μm	...	244 ± 5	*Spitzer*/IRAC
24. μm	6.95 μm	...	1099 ± 18	*Spitzer*/MIPS
1.4 GHz	4.95 GHz	...	<162	VLA

LRIS (Oke et al. 1995) on the Keck I telescope. The observations were taken in multiobject mode, and three equal integrations were performed for a total exposure time of 1.5 hr. The observations were taken with 1.″5 wide slitlets aligned near the parallactic angle. The effective wavelength range of the blue spectrograph of the instrument is 3500–6700 Å. A 300 line mm^{-1} grism with a blaze wavelength of 5000 Å was used, resulting in 1.43 Å pixel^{-1} dispersion. We used an HgAr lamp spectrum obtained at the same position angle immediately following the observations for wavelength calibration. The night was photometric with ~1.″3 seeing, and the spectra were calibrated using the observations of the standard star G191-B2B from Massey et al. (1988). The spectra of SW 104409 and SW 104406 are shown in Figures 6 and 7, respectively. The optical flux and spectral shape of SW 104409 and SW 104406 at the time of the Keck observations are consistent, within 1 σ, with the earlier broadband g' and r' photometric measurements.

The spectrum of SW 104409 shows a narrow (FWHM = 1324 ± 80 km s^{-1}) Lyα emission line and two asymmetric emission lines with a broad blueward component, C IV λ1549 and N V λ1240. The spectrum of SW 104406 shows several narrow emission lines, e.g., Lyα with FWHM = 1360 ± 20 km s^{-1} and C IV λ1549 with FWHM = 1485 ± 60 km s^{-1}. The line identifications and parameters (FWHM, fluxes, and the rest-frame equivalent width $W_{\lambda,\mathrm{rest}}$), calculated for single-Gaussian fits using IRAF (Kriss 1994), are listed in Tables 8 and 9. In the case of SW 104409, since the signal-to-noise ratio is too low to constrain a Gaussian fit for the broad component of the asymmetric emission lines, the total flux and equivalent width were derived by integrating the total spectrum around the lines and subtracting the continuum (see Table 8). The estimated mean redshifts are 2.54 ± 0.02 for SW 104409 and 2.430 ± 0.003 for SW 104406.

According to the properties of its optical spectrum, SW 104406 is a classical type 2 QSO, while SW 104409 could be considered a peculiar type 2 QSO because of the superposition of weak asymmetric broad components on top of the stronger narrow emission lines.

A more detailed analysis and an in-depth investigation of the spectrum of SW 104409 are beyond the scope of this work. The blueshifted broad components of the C IV λ1549 and N V λ1240 emission lines suggest the presence of highly ionized gas moving toward the observer as an outflow or wind from the accretion disk as observed in other quasars (Gallagher et al. 2005).

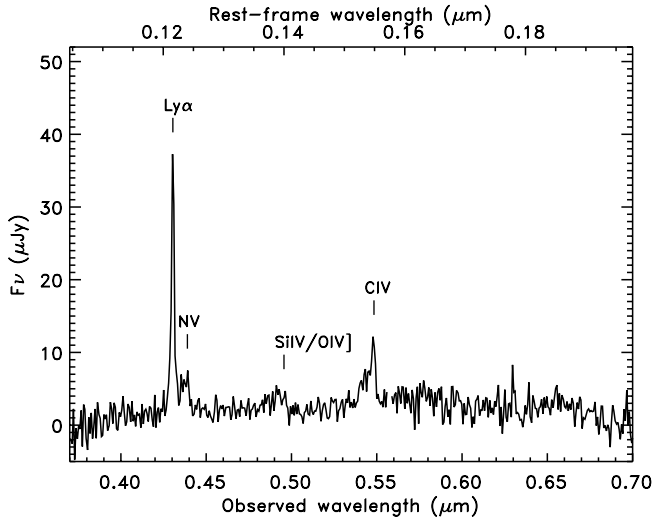

FIG. 6.—Optical spectrum of SW 104409 obtained with the Keck I telescope. Detected emission features are labeled.

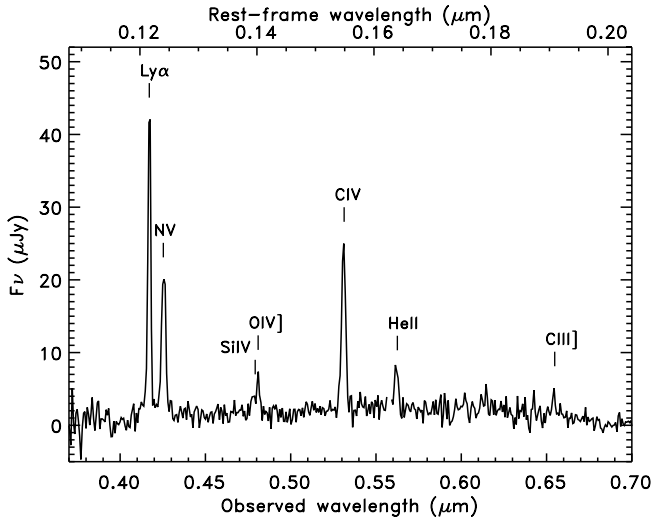

FIG. 7.—Optical spectrum of SW 104406 obtained with the Keck I telescope. Detected emission features are labeled.

TABLE 8
EMISSION-LINE MEASUREMENTS OF SW 104409

Line	λ_{obs} (Å)	Redshift	Flux (10^{-16} ergs cm^{-2} s^{-1})	FWHM (km s^{-1})	$W_{\lambda,rest}$ (Å)
Lyα[a]	4304.5	2.540	12.5 ± 1.3	1324 ± 80	105 ± 11
N v λ1240[a]	4389.5	2.540	1.88 ± 0.56	1366 ± 300	16 ± 5
C iv λ1549[a]	5479.3	2.537	2.23 ± 0.45	1367 ± 200	21 ± 4
Lyα/N v λ1240[b]	...	...	23.0 ± 2.3	...	311 ± 31
Si iv/O iv] λ1400[b]	...	...	2.34 ± 0.47	...	29 ± 6
C iv λ1549[b]	...	...	4.15 ± 0.62	...	39 ± 6

NOTE.—Rest-frame equivalent widths $W_{\lambda,rest}$ assume $z = 2.54$.
[a] Gaussian fit to narrow component.
[b] Total integration.

However, this interpretation is difficult to reconcile with a geometry in which the AGN is obscured.

4.2. *X-Ray Data and Spectral Analysis*

Details (sequence number, observation ID, and exposure time) on the X-ray observations of SW 104409 and SW 104406 are listed in Table 10. SW 104409, located at an off-axis angle of 3.′6, has 11 broadband counts, only 2 of which fall in the soft band. SW 104406, at an off-axis angle of 5.′8, is brighter in the X-ray than SW 104409 with 22 broadband counts, of which 3 fall in the soft band. With so few counts, the error on the source's hardness ratio is large and spectral modeling would not constrain any parameter. Therefore, in order to constrain the amount of absorption in these sources, we applied the Bayesian method described in § 2.2 (van Dyk et al. 2004). We derive an HR of $0.85^{+0.06}_{-0.39}$ for SW 104409 and $0.61^{+0.21}_{-0.23}$ for SW 104406, which correspond to intrinsic column densities of $2.0^{+0.5}_{-1.3} \times 10^{24}$ cm^{-2} for SW 104409 and $1.0^{+0.7}_{-0.3} \times 10^{24}$ cm^{-2} for SW 104406. These extreme column densities indicate that both sources are borderline Compton-thick AGNs. Alternative models, such as a reflection component due to ionized or neutral gas, cannot be ruled out, but they would also indicate large column densities ($\sim 10^{24}$ cm^{-2}). Assuming that the X-ray spectra of SW 104409 and SW 104406 are due to transmitted components through column densities of $N_H = 2 \times 10^{24}$ and 1×10^{24} cm^{-2}, respectively, the absorption-corrected X-ray luminosities in the rest frame, assuming a photon index $\Gamma = 1.7$, are 4×10^{45} and 5×10^{45} ergs s^{-1}, respectively.

4.3. *Radio Data*

SW 104409, located at 17′ from the center of the radio field, is unresolved but clearly detected. Its radio flux, measured on an image convolved to 3″ to reduce instrumental effects this far off-axis, is 273 ± 15 μJy. SW 104406, located at the edge of the radio field (26′ off-axis), is not detected in the radio (there is only an apparent 2.4 σ detection); therefore, we assume a 3 σ upper limit to its radio flux of 162 μJy.

5. SPECTRAL ENERGY DISTRIBUTIONS OF SW 104409 AND SW 104406

In this section we analyze the SEDs from X-ray to radio wavelengths of the two obscured quasars discussed above, SW 104409 and SW 104406. The SED shapes and luminosities are compared to those of known AGNs: the Elvis QSO template and the BAL QSO/Seyfert 1 galaxy Mrk 231. The SEDs are interpreted assuming the unification scenario for which the absorbing material is distributed around the central source in a toroidal shape. However, alternative models cannot be ruled out by the available data.

5.1. *SW 104409*

The SED of SW 104409, from X-ray to radio wavelengths, is shown in Figure 8 and compared to the SED of Mrk 231. SW 104409 is characterized by a blue optical spectrum up to 2200 Å in the source rest frame, followed by a rapid rise at longer wavelengths with an observed $r' - K_s = 4.13$ (Vega), fitting the conventional definition of extremely red objects (EROs; $R - K > 4$; Elston et al. 1988). The U-band dropout is probably due to intergalactic medium (IGM) attenuation (Madau 1995), as expected for such a high-redshift object. The comparison with Mrk 231 shows how extreme the IR SED of SW 104409 is [$F^{rest}\nu(2.2\ \mu m)/F^{rest}\nu(0.6\ \mu m) = 94$ compared to 9.7 for Mrk 231]. However, the mid-IR (10 μm)/radio flux ratios are very similar, and the mid-IR (10 μm)/X-ray flux is only 3 times higher in SW 104409 than in Mrk 231.

The X-ray and near-IR properties of SW 104409 indicate that the source is heavily obscured. However, the observed optical continuum is blue and the spectrum shows emission lines with broad components. A plausible explanation for the observed optical spectrum could be scattering. The scattered light preserves

TABLE 9
EMISSION-LINE MEASUREMENTS OF SW 104406

Line	λ_{obs} (Å)	Redshift	Flux (10^{-16} ergs cm^{-2} s^{-1})	FWHM (km s^{-1})	$W_{\lambda,rest}$ (Å)
Lyα	4171.3	2.431	14.9 ± 1.5	1360 ± 20	184 ± 18
N v λ1240	4254.8	2.431	9.82 ± 0.29	2037 ± 40	120 ± 4
Si iv λ1397	4777.4	2.430	1.15 ± 0.35	1684 ± 200	16 ± 5
O iv] λ1402	4809.4	2.430	1.23 ± 0.12	1120 ± 100	17 ± 2
C iv λ1549	5310.7	2.428	7.14 ± 0.14	1485 ± 60	86 ± 2
He ii λ1640	5618.9	2.425	1.50 ± 0.08	1278 ± 100	20 ± 1

NOTES.—All parameters are derived for Gaussian fits. Rest-frame equivalent widths $W_{\lambda,rest}$ assume $z = 2.43$.

TABLE 10
X-Ray Observational Details

Source Name	Sequence Number	ObsID	Date	Exposure Time (ks)
SW 104406.....	900331	5024	2004 Sep 16	57.97
SW 104409.....	900334	5027	2004 Sep 20	67.96

the spectral shape of the intrinsic component, but its flux corresponds to a fraction of the primary component that depends on the covering factor of the scattering medium (Smith et al. 2003). The fraction of scattered radiation can be estimated by comparing the observed and the intrinsic (unabsorbed) optical flux. Since the observed optical spectrum is similar to that observed in optically selected quasars and scattering does not modify the spectral shape of the intrinsic spectrum, we estimated the intrinsic optical flux by assuming that the intrinsic (before absorption) SED of SW 104409 is similar to that of an unobscured QSO normalized at the observed mid-IR observed flux. In Figure 9 we show the SED of SW 104409 and an unobscured QSO template in three cases: (1) normalized at the observed 24 μm flux of SW 104409, to represent the intrinsic (before absorption) emission of SW 104409; (2) scaled to match the observed optical data, to represent the scattered component; and (3) reddened by an extinction $A_V = 4$ mag [$E(B-V) \simeq 1$]. Reddening was applied as prescribed in Calzetti & Heckman (1999) assuming a foreground screen of dust at the redshift of the source. According to this scenario, SW 104409 resembles an optically selected quasar whose light is reddened by an extinction $A_V = 4$ mag and, therefore, completely suppressed at the observed optical wavelengths (ultraviolet in the rest frame) and reddened in the near-IR (optical in the rest frame). Assuming that the observed optical blue spectrum is due to scattering, the scattered fraction corresponds to 0.6% of the intrinsic optical emission.

Note that throughout this work we apply reddening as prescribed in Calzetti & Heckman (1999). We also investigated the use of the Small Magellanic Cloud (SMC) extinction curve (Prevot et al. 1984; Bouchet et al. 1985) that well reproduces the optical spectra of dust-reddened quasars in SDSS (Richards et al. 2003). The two prescriptions produce similar reddening at $\lambda > 5000$ Å, but the SMC law produces redder spectra at shorter wavelengths for the same amount of extinction.

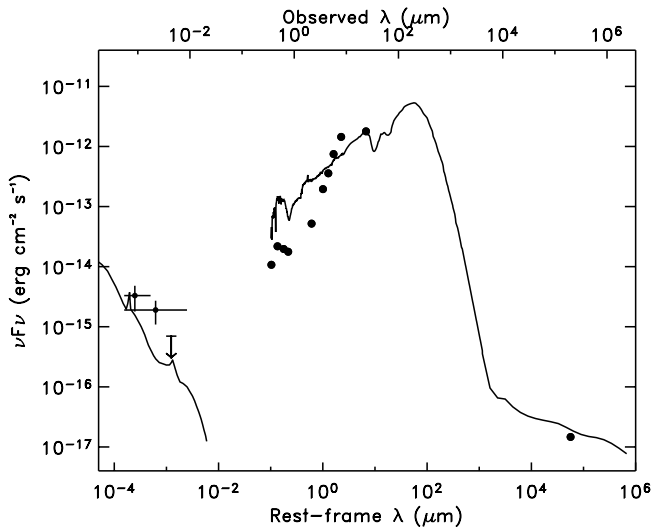

FIG. 8.—SED of SW 104409 (*filled circles*) compared to the SEDs of the Compton-thick AGN (*solid line*), Mrk 231, normalized at the observed 24 μm flux. The crosses correspond to the observed X-ray flux in the broad and hard X-ray bands. The downward-pointing arrow is the 2 σ upper limit to the soft X-ray flux. The X-ray flux energy range is indicated by the length of the horizontal line. The X-ray fluxes are derived assuming an absorbed power-law model with photon index Γ equal to 1.7 and Galactic absorption $N_H = 6 \times 10^{19}$ cm^{-2}.

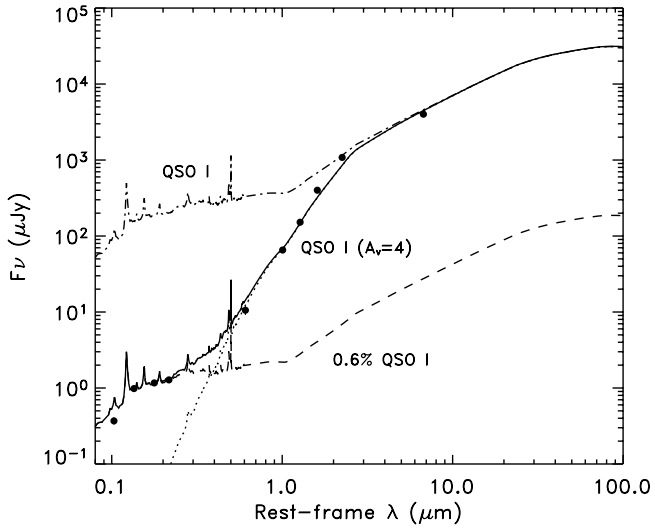

FIG. 9.—Observed SED of SW 104409 (*filled circles*) compared to an unobscured QSO template: (1) normalized to the mid-IR flux of SW 104409 (*dot-dashed line*), (2) scaled to match the optical flux of SW 104409 (*dashed line*), and (3) extinguished by $A_V = 4$ to fit the IR data points (*solid line*; see § 4.1). The solid line corresponds to the sum of the extinguished (item 3) and the scattered components (item 2).

Different geometries of the obscuring material were investigated by comparing the observed SED of SW 104409 with predictions from radiative transfer models within the AGN unification scenarios. The models assume that the absorbing material is distributed in a toroidal shape around the central heating source. Two geometries were taken into account, flared and tapered disks, as described in detail in Efstathiou & Rowan-Robinson (1995). In flared disks the thickness of the disk increases linearly with distance from the central source. In tapered disks the thickness of the disk in the inner part also increases linearly with distance from the source but stays constant in the outer part. We find that a good fit to the rest-frame ultraviolet to mid-IR spectrum of SW 104409 can be obtained with a tapered disk with an opening angle of 60°. The predicted SED for this model is shown in Figure 10 and compared to the observed SED of SW 104409. The predicted inclination of the line of sight with respect to the disk axis (61°) implies that it is almost grazing the boundaries of the torus. The line-of-sight optical depth at 1000 Å rest frame through the torus is 700, which corresponds to an optical depth $\tau_V = 129$ or $A_V = 140$. The best-fit model also assumes that the emission from the torus suffers additional extinction of 0.5 mag by dust that is located at some distance from the nucleus, e.g., in the host galaxy. The predicted optical emission, which agrees well with the observed optical data, is produced by light scattered by the torus.

Due to the high optical depth to the central source, the optical emission must be scattered light. According to this model, scattering takes place in the inner walls of the disk and its surface; therefore, in order to observe scattered light, the inclination must be slightly larger than the opening angle of the disk. In the case of larger inclination angles, the disk would obscure the scattered light. For inclination angles smaller than the opening angle, the scattered light would still be visible; however, this geometry would be inconsistent with the obscured nature of this source.

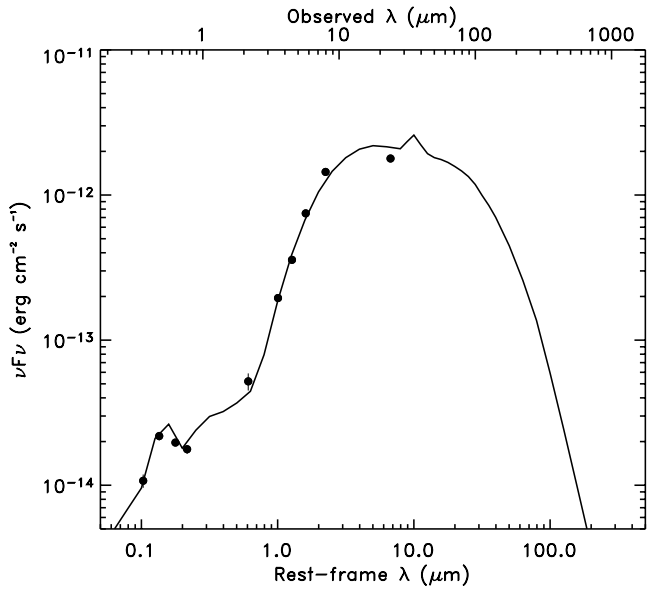

FIG. 10.—Observed SED of SW 104409 (*filled circles*) compared to a model of tapered disk with opening angle of 60°, optical depth $\tau_V = 129$, and line-of-sight inclination of 61° (*solid line*).

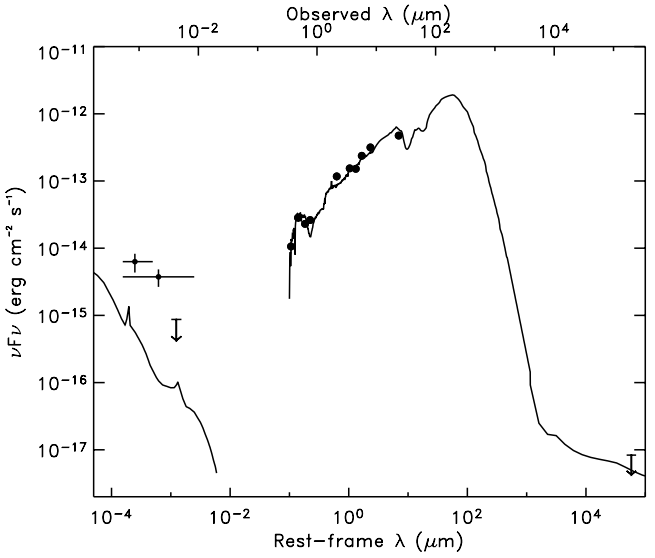

FIG. 11.—SED of SW 104406 (*filled circles*) compared to the SED of the Compton-thick Seyfert 1 Mrk 231 normalized at 24 μm with an $A_V = 0.2$ mag additional extinction (*solid line*). The crosses correspond to the observed X-ray flux in the broad and hard X-ray bands. The downward-pointing arrow is the 2 σ upper limit to the soft X-ray flux. The X-ray flux energy range is indicated by the length of the horizontal line. The X-ray fluxes are derived assuming an absorbed power-law model with photon index Γ equal to 1.7 and Galactic absorption $N_H = 6 \times 10^{19}$ cm^{-2}.

The similarity between the inclination and opening angles is also suggested by the observed 1–10 μm SED, characteristic of emission from hot dust. Since the scattering region and the hot dust region are almost cospatial, the inclination must be similar to the opening angle; otherwise, the disk would obscure the emission from this region. An alternative to this model is scattering produced by electrons or dust in the opening cone of the accretion disk, instead of from the walls of the disk. In this case the similarity between the opening and inclination angles is not required; however, it would still be required to explain the shape of the near- to mid-IR continuum. This model is consistent with the simple scenario described above. The large difference in the amount of extinction is likely due to the different assumptions made for the dust distribution. In the simple "scattering + obscured QSO" model, we assume a foreground screen of dust absorbing the emitted radiation. This assumption does not take into account reemission from dust and produces an underestimation of the dust opacity. Radiative transfer models are more accurate in estimating the dust opacity since they take into account the transmission of the intrinsic radiation through the dusty material. According to the results from the radiative transfer model and assuming a Galactic dust-to-gas ratio, the estimated gas column density surrounding the central regions is $\sim 2.6 \times 10^{23}$ cm^{-2}, consistent with what is observed in the X-ray. However, since the X-ray emission is produced in the nucleus and the optical and near-IR radiation is emitted in the outer regions, the absorbing gas intercepted by the X-ray photons is expected to be closer to the disk plane and have a larger column density than the material intercepted by the optical/near-IR radiation. In spite of its simplicity, the proposed picture reconciles the multiwavelength observations of SW 104409 and agrees well with the unification model.

5.2. *SW 104406*

The SED of SW 104406 is shown in Figure 11. The optical spectrum is characterized by a blue continuum as in the case of SW 104409 with no indication for intrinsic reddening. As in the case of SW 104409, the optical data are characterized by a *U*-band dropout that is probably caused by IGM attenuation. SW 104406 also fits within the conventional definition of EROs with an observed $r' - K_s = 4.82$ (Vega). Its SED is very similar to the SED of Mrk 231 after applying an additional extinction of $A_V = 0.2$ as shown in Figure 12. The optical spectrum can be fitted with this reddened template, and an additional component, such as scattered light, is not required by the data. The X-ray/IR ratio of SW 104406 is about 10 times higher than for Mrk 231, but the X-ray spectrum is similarly hard or even harder. Contamination from stellar light emission from the host galaxy or a

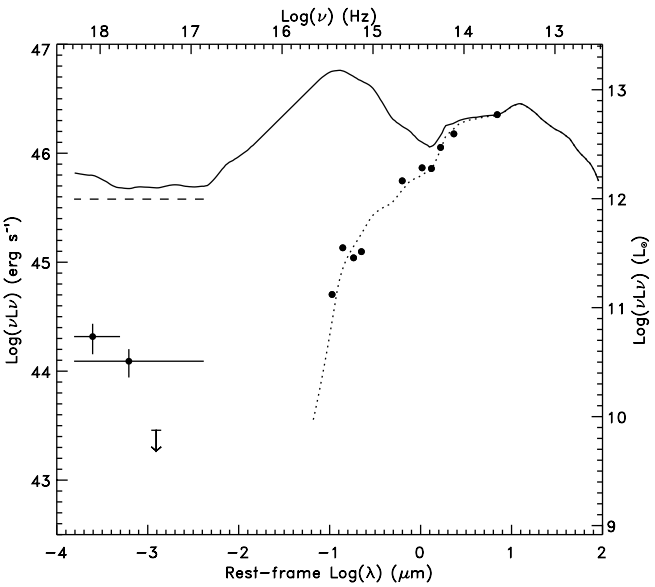

FIG. 12.—SED in $\nu L\nu$ of SW 104406 (*filled circles*) compared to the Elvis QSO template normalized at 24 μm in two cases: (1) with no additional extinction (*solid line*) and (2) with 1.7 mag additional extinction (*dotted line*). The dashed line corresponds to the absorption-corrected broadband X-ray luminosity. The crosses correspond to the X-ray luminosities in the broad and hard X-ray bands. The downward-pointing arrow is the 2 σ upper limit to the soft X-ray luminosity. The X-ray energy range is indicated by the length of the horizontal lines.

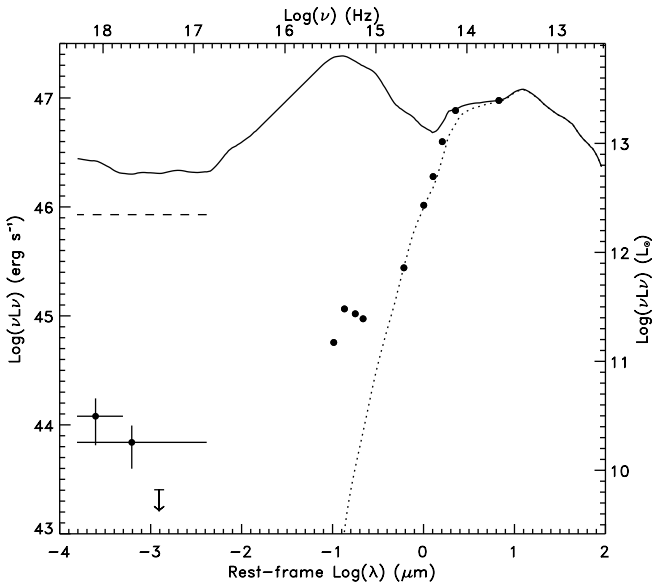

FIG. 13.—SED in $\nu L\nu$ of SW 104409 (*filled circles*) compared to the Elvis QSO template normalized at 24 μm in two cases: (1) with no additional extinction (*solid line*) and (2) with 4.0 mag additional extinction (*dotted line*). The dashed line corresponds to the absorption-corrected broadband X-ray luminosity.

starburst, which would appear as a broad bump with a peak at $\lambda^{\rm rest} \sim 1.6$ μm, is not observed.

In summary, both sources show SEDs where the AGN dominates at all observed wavelengths and any contribution from another energy source is negligible. The observed SEDs are both consistent with a scenario in which the optical and near-IR sources are obscured. In the X-rays, the observed spectrum is likely due to the transmitted direct component seen through Compton-thick matter.

6. LUMINOSITY, BLACK HOLE MASS, AND ACCRETION RATE OF SW 104409 AND SW 104406

The luminosities as a function of wavelength of SW 104406 and SW 104409 are shown in Figures 12 and 13, respectively. The luminosity distribution of the unobscured quasar template, Elvis QSO (Elvis et al. 1994), normalized to the mid-IR flux of the two quasars is also shown for comparison. The template is also shown after applying enough extinction to reproduce the red IR SEDs of SW 104409 and SW 104406.

Due to the lack of data at $\lambda_{\rm rest} > 7$ μm, we cannot directly measure the total IR luminosity, but we can derive it making some assumptions about the SED shape. Assuming the model shown in Figure 9 for SW 104409 and a reddened ($A_V = 0.2$) Mrk 231 for SW 104406 at $\lambda = 7-1000$ μm, the IR luminosities, L(3–1000 μm), are 3.4×10^{47} (=8.8×10^{13} $L_\odot$) and 1.2×10^{46} ergs s^{-1} (=3.1×10^{12} $L_\odot$), respectively. SW 104409 is a hyperluminous infrared galaxy (HyLIRG) and SW 104406 an ultraluminous infrared galaxy (ULIRG; Sanders & Mirabel 1996). The integrated luminosities in different wavelength ranges, as well as the bolometric luminosity of both sources, are listed in Table 11. The radio luminosity is derived assuming the radio spectral index typically observed in AGNs, $\alpha = -0.8$ (Condon 1988), where $F_\nu \propto \nu^\alpha$. The implied rest-frame 1.4 GHz radio luminosity density is $L_{1.4\ {\rm GHz}} = 5.3 \times 10^{31}$ ergs s^{-1} Hz^{-1} for SW 104409 and less than 3.0×10^{31} ergs s^{-1} Hz^{-1} for SW 104406. These high radio powers are a signature of the presence of an AGN.

The bolometric luminosity can be derived by adding the absorption-corrected X-ray luminosity, the estimated radio luminosity (only in the case of SW 104409), and the optical–IR luminosity. The derived bolometric luminosities are 3.9×10^{47} ergs s^{-1} (1.0×10^{14} $L_\odot$) for SW 104409 and 1.9×10^{46} ergs s^{-1} (4.6×10^{12} $L_\odot$) for SW 104406. Because of the uncertainty associated with the lack of data above $\lambda^{\rm rest} = 7$ μm, we derived a lower limit to the bolometric luminosity by replacing the optical–IR luminosity L(0.03–1000 μm) with L(0.03–10 μm). The obtained values are a factor of 2 lower than the estimates obtained by extrapolating the model to $\lambda > 10$ μm (see values in Table 11). The absorption-corrected X-ray luminosities of SW 104409 and SW 104406 correspond, respectively, to ~1% and 30% of their bolometric luminosity.

Assuming that the AGN is the main source of the observed bolometric luminosity and that it is accreting at the Eddington limit ($L_{\rm bol} = L_{\rm Edd}$), the estimated black hole mass for SW 104409 and SW 104406 is $\simeq 2.9 \times 10^9$ and 1.4×10^8 $M_\odot$, respectively, or 1.2×10^9 and 6.6×10^7 $M_\odot$, if we do not include the energy emitted at $\lambda > 10$ μm in the estimate of the AGN bolometric luminosity. If we assume an accretion efficiency of 10%, the derived accretion rates are 68 $M_\odot$ yr^{-1} for SW 104409 and 3.4 $M_\odot$ yr^{-1} for SW 104406, or 28 $M_\odot$ yr^{-1} for SW 104409 and 1.5 $M_\odot$ yr^{-1} for SW 104406 if we do not include the energy emitted at $\lambda > 10$ μm in the estimate of the AGN bolometric luminosity. The black hole mass of SW 104409 is comparable to the highest measured values in the local universe, i.e., M87 (Ford et al. 1994) and Cyg A (Tadhunter et al. 2003), having $M_{\rm BH} \simeq 3 \times 10^9$ $M_\odot$. Its accretion rate is also among the highest observed in quasars at $z \leq 2$ (McLure & Dunlop 2004). SW 104406 is also characterized by a large black hole mass and accretion rate, but it is not as extreme as SW 104409. Since most of the quasars accrete

TABLE 11

LUMINOSITIES AND BLACK HOLE MASSES OF SW 104409 AND SW 104406

Source Name	$L_{\rm radio}$ (1.4 GHz)	L(O–NIR)[a] (0.03–10 μm)	L(IR)[a] (3–1000μm)	L(O–IR)[a] (0.03–1000μm)	L(X)[b] (0.3–8 keV)	$L_{\rm bol}$[c]	$M_{\rm BH}$[d] (10^8 $M_\odot$)	dM/dt[e] ($M_\odot$ yr^{-1})
SW 104406	<40.07	45.48	46.08	46.14	45.74	46.29 (45.93)	1.4 (0.7)	3.4 (1.5)
SW 104409	40.32	47.19	47.53	47.58	45.64	47.59 (47.21)	29.9 (12.4)	68 (28)

NOTES.—All luminosities are in logarithmic scale and units of ergs s^{-1}. See § 6 for more details.

[a] Derived assuming the model shown in Fig. 9 for SW 104409 and in Fig. 11 for SW 104406.

[b] Absorption-corrected X-ray luminosity between 0.3 and 8 keV.

[c] Bolometric luminosity derived as the sum of L(O–IR), L(0.3–8 keV), and L(radio) if available. The value in parentheses does not include the luminosity emitted at $\lambda^{\rm rest} > 10$ μm and was obtained by replacing L(O–IR) with L(O–NIR) in the $L_{\rm bol}$ calculation.

[d] Black hole mass derived from $L_{\rm bol}$ and assuming that the source is accreting at the Eddington limit. The value in parentheses was derived using the $L_{\rm bol}$ value shown in parentheses in the seventh column.

[e] Accretion rate derived from $L_{\rm bol}$ and assuming that the source is accreting with 10% efficiency. The value in parentheses was derived using the $L_{\rm bol}$ value shown in parentheses in the seventh column.

below their Eddington limit (McLure & Dunlop 2004), it would be more realistic to assume a lower Eddington ratio; however, this would imply even higher black hole masses.

7. COMPARISON WITH OTHER COMPTON-THICK AGNs AT $z \gtrsim 2$

Only a few Compton-thick quasars at $z \gtrsim 2$ are currently known. Here we compare their properties with those of SW 104409 and SW 104406 and investigate whether they represent the same population or if the different selection methods are finding objects with different properties. The largest and probably best sampled sample of Compton-thick AGNs currently known contains four sources (Alexander et al. 2005a, 2005b). These sources were drawn from an X-ray–detected, submillimeter-selected sample in a 0.12 deg^2 field. Optical data from the *Hubble Space Telescope* (*HST*), IR data from *Spitzer*, radio data, and optical high-resolution spectra are available for all of the sources. Spectroscopic redshifts range from 2 to 2.5, and broad-band (0.5–8 keV) X-ray fluxes range from 0.7×10^{-15} to 1.3×10^{-15} ergs cm^{-2} s^{-1}. These sources host both an AGN and a powerful starburst, and their optical–near-IR SEDs are dominated by stellar light (Borys et al. 2005). The optical spectra of all sources are also dominated by a starburst component (Chapman et al. 2005). The AGN bolometric luminosities, estimated from the observed X-ray flux after correcting it for absorption, range from 2.2×10^{11} to 4.4×10^{11} $L_\odot$, the derived black hole masses range from 0.6×10^7 to 1.6×10^7 $M_\odot$, and the accretion rates vary from 0.13 to 0.35 $M_\odot$ yr^{-1}. The main differences between this sample and the two obscured quasars SW 1044090 and SW 104406 are in the AGN bolometric luminosity and thus in the accretion rates and the black hole masses, which are, on average, 2 orders of magnitude lower. Another important difference is the presence of a dominant starburst component, which is absent or negligible in SW 104409 and SW 104406. It is clear that the two quasars presented in this work and these AGN/submillimeter galaxies show some major differences and might be very different objects. However, before deriving any conclusions on the differences between these two samples, we should evaluate how the different methods applied to estimate the AGN bolometric luminosity affect these results.

We tried to reproduce the Alexander et al. (2005b) estimates using their energy ranges and found that their correction for absorption to the rest-frame X-ray luminosity is about 4 times smaller than ours for $N_{\rm H} = 10^{24}$ cm^{-2}. The most likely explanation for the observed difference is the difference in the assumed X-ray model used to derive the *K*-correction. Alexander et al. (2005a, 2005b) adopt a model that includes an absorbed power-law component with $\Gamma = 1.8$, a neutral reflection component, a scattered component of ionized gas, and an Fe Kα emission line at 6.4 keV. We also notice a discrepancy in the column density estimates, their values being on average 2.5 times larger than what we would predict with our method. Although this would yield larger luminosities, their correction factor due to the different spectral model is much smaller than ours; thus, their absorption-corrected rest-frame luminosities are lower that what we would estimate. If we apply our method to their sample, the derived absorption-corrected rest-frame X-ray luminosities are, on average, higher by a factor of 8 (from 3 to 12.5 times higher). Their smaller X-ray luminosities imply smaller AGN bolometric luminosities, black hole masses, and accretion rates by the same factors. A third difference between our methods is in the derivation of bolometric luminosity. They assume a constant factor between the absorption-corrected rest-frame X-ray luminosity and the bolometric luminosity of 6%, while we add the luminosity measured throughout the whole spectrum (30% for SW 104409 and 1% for SW 104406; see § 6). Even after correcting by the factors described above, the differences in AGN luminosity, SMBH mass, and accretion rate between the two quasars presented in this work and the sample in Alexander et al. (2005a, 2005b) are still significant, more than 1 order of magnitude compared to almost 2 orders of magnitude initially measured. Thus, we conclude that the four sources in Alexander et al. (2005b) and our two quasars are different.

Other examples of Compton-thick AGNs at high z are the type 2 quasars, CXO 52 ($z = 3.288$; Stern et al. 2002), CDFS 202 ($z = 3.700$; Norman et al. 2002), and CDFS 263 ($z = 3.660$; Mainieri et al. 2005). The former two sources show similar characteristics to SW 104409 and SW 104406. The X-ray–selected type 2 QSO detected at submillimeter wavelengths, CDFS 263, is instead more similar to the submillimeter-selected AGN discussed above. The SEDs of these quasars at $\lambda > 2.5$ μm are not currently available, but at shorter wavelengths CXO 52 and CDFS 202 show very similar SEDs to those of SW 104409 and SW 104406 with AGN-dominated optical spectra and red optical–near-IR colors. Assuming that the absorption-corrected X-ray luminosity corresponds to 10% of the AGN bolometric luminosity (Elvis et al. 1994), we derive a bolometric luminosity, $L_{\rm bol}$, of 3.3×10^{45} ergs s^{-1} for CXO 52 and 2×10^{46} ergs s^{-1} for CDFS 202. Assuming accretion at the Eddington limit, the black hole masses are 2.5×10^7 and 1.1×10^8 $M_\odot$, respectively. These values are also lower than what we derive for SW 104409 and similar to those derived for SW 104406, but higher than those measured in the Alexander et al. (2005a) submillimeter-selected Compton-thick AGNs. In CXO 52 and CDFS 202, as in SW 104409 and SW 104406, the AGN dominates over the host galaxy and the associated luminosity and SMBH mass are 1 order of magnitude higher than observed in submillimeter-selected Compton-thick AGNs.

The two Compton-thick AGNs discussed in this work also differ from a sample of high-z, heavily obscured, luminous AGN candidates selected at IR and radio wavelength (Martínez-Sansigre et al. 2005). We applied the same selection criteria to the complete IR and X-ray samples, to the IR-selected obscured AGN candidates, and to the X-ray–selected Compton-thick AGNs in Figure 14. Only one source among the IR-selected obscured AGN candidates satisfies their selection criteria, SWIRE J104641.38+585213.9, and none of the X-ray-selected Compton-thick AGNs do. Although the two Compton-thick AGNs, SW 104409 and SW 104406, are luminous and obscured AGNs at $z > 2$ (see § 4), they do not pass either the 3.6 μm or the radio limit (see large black circles in Fig. 14) required by Martínez-Sansigre et al. (2005). In the entire field only six sources satisfy their selection criteria, of which two show power-law–like IR SEDs and are also detected in the X-ray. One is SWIRE J104641.38+585213.9, which we classify as a class III source (see Table 4); the other source is characterized by an SED consistent with an unobscured QSO. The remaining four sources are characterized by SEDs more similar to those in class IV. Although both selection methods are based on IR colors derived from *Spitzer*, there is little overlap among the two samples.

A compilation of all heavily obscured AGNs selected by different methods and a systematic analysis of their multiwavelength properties is necessary to understand the differences among these sources and their origin, e.g., a different evolutionary stage, SMBH mass, accretion rate, or environment.

8. STATISTICAL PREDICTIONS FOR COMPTON-THICK AGNs

The two selection methods described in §§ 3.1 and 3.2 were defined for samples of obscured AGNs based on their X-ray and

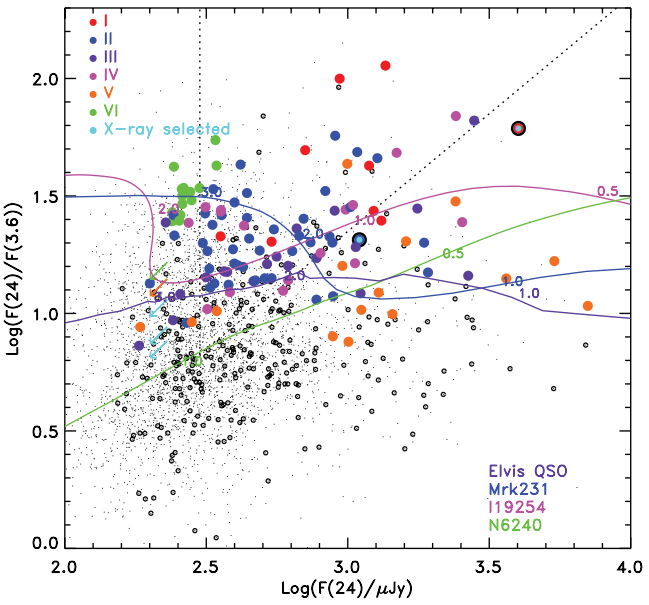

FIG. 14.—IR color $F(24\ \mu\mathrm{m})/F(3.6\ \mu\mathrm{m})$ vs. the IR flux at 24 μm for the IR (*black dots*) and X-ray (*black open circles*) sources detected at 3.6 and 24 μm in the *Chandra*/SWIRE field. IR-selected obscured AGN candidates are shown as filled circles with colors corresponding to different SED types (*red*: I; *blue*: II; *purple*: III; *magenta*: IV; *orange*: V; *green*: VI). Symbols as in Fig. 4. X-ray–selected obscured AGNs are shown as cyan filled circles and as cyan arrows if nondetected at 24 μm. The dotted line defines the IR selection criteria used in Martínez-Sansigre et al. (2005) for obscured AGNs at high z.

optical–IR properties, respectively. The X-ray–selected sample includes X-ray–detected AGNs with hard X-ray spectra and estimated column densities $\geq 10^{24}$ cm^{-2} (five sources). The IR-selected sample contains AGNs with red optical–IR colors and whose emission dominates in the near- and mid-IR over the host galaxy light (120 sources). The first selection method is biased against Compton-thick AGNs whose primary X-ray radiation is completely absorbed in the observed energy range, i.e., sources at low z or with column densities $\geq 10^{25}$ cm^{-2}, and against sources that are fainter than 10^{-15} ergs cm^{-2} s^{-1} at 0.3–8 keV. The second method is biased against AGNs that are too faint to be detected in three IR bands at our sensitivity limits or whose host galaxy is brighter than the AGNs in the optical–IR wavelength range. Because of these selection effects, we can only estimate a lower limit to the surface density of IR-detected Compton-thick AGNs in the *Chandra*/SWIRE field.

In the subsample of 41 IR-selected obscured AGN candidates that are detected in the X-rays, only 2 sources (~5%) are confirmed Compton-thick AGNs, SW 104409 and SW 104406. If we assume that this fraction does not depend on the X-ray flux and is the same for the entire IR-selected sample of obscured AGN candidates (but see discussion in § 3.2.3), we estimate about 6 sources (5% of 120 sources) to be Compton-thick AGNs. Since only two out of five X-ray–selected Compton-thick AGNs are also selected by the IR-selected criteria, we assume that our IR selection identifies only 40% (two out of five) of all Compton-thick AGNs in the field. Thus, the estimated total number of Compton-thick AGNs in the field is about 15 (≃6/0.4), or 25 sources deg^{-2}. The estimated number of sources (15) should be considered a lower limit to the total number of Compton-thick AGNs detected in the IR at our sensitivity limits in the *Chandra*/SWIRE field. Due to the lack of X-ray data for most of the sources, the identification of these 15 Compton-thick AGNs is not possible because of a lack of constraints on their column densities. The only exceptions are the five X-ray–selected Compton-thick AGNs presented in § 3.1. The fraction of Compton-thick AGNs detected in the X-ray at our depth [$F(0.3-8\ \mathrm{keV}) \geq 10^{-15}$ ergs cm^{-2} s^{-1}] is 33% (5 out of 15). This fraction is consistent with the value estimated by Treister et al. (2004) of 30% of all Compton-thick AGNs detected at the X-ray limit of the *Chandra* deep surveys.

We compared our results with the number of obscured AGNs detected in the IR and in the X-rays predicted by various models (Silva et al. 2004; Treister & Urry 2005; Xu et al. 2003; Polletta et al. 2003). Since our selection is very similar to a 24 μm flux selection, we compared our results with those predicted for AGNs with a 24 μm flux greater than our 5 σ limit, 230 μJy. However, our selection is more restricted due to the additional requirements on the properties of the IR SED; therefore, we expect our numbers to be lower than those expected from a limited flux sample of AGNs. Silva et al. (2004) predict about 670 AGNs deg^{-2}, of which 500 are obscured ($N_{\mathrm{H}} \geq 10^{22}$ cm^{-2}; obscured : unobscured = 2.9 : 1) and about 300 are Compton thick. Treister & Urry (2005) predict about 1000 AGNs deg^{-2}, of which 765 are obscured ($N_{\mathrm{H}} \geq 10^{22}$ cm^{-2}; obscured : unobscured = 3 : 1) and no prediction for Compton-thick AGNs is given. Xu et al. (2003) and Polletta et al. (2003) predict about 1100 AGNs deg^{-2}, of which 810 are obscured ($N_{\mathrm{H}} \geq 10^{22}$ cm^{-2}; obscured:unobscured = 2.8:1). Although these models are different and have not been fully tested with respect to the available IR and X-ray observables, they are all consistent with a surface density of about 700–1000 AGNs deg^{-2}, a ratio between obscured and unobscured AGNs of 3 : 1, and about 300 Compton-thick AGNs. Our IR selection of AGNs yields 120 (~200 deg^{-2}) obscured AGN candidates and 61 (~100 deg^{-2}) unobscured AGN candidates, corresponding to only about 20% of the expected number of AGNs and to an obscured : unobscured ratio of ~2 : 1. The total number of AGNs and the ratio between obscured and unobscured AGNs would likely increase if the selection was not limited to sources with AGN-dominated and red IR SEDs. Our lower limit to the surface density of Compton-thick AGNs is less than 10% of the expected value, indicating that even in the mid-IR a large fraction of these sources are elusive.

9. CONCLUSIONS

Theoretical models, simulations, and indirect observations predict the presence of a large population of highly obscured luminous AGNs at moderate and high redshifts. The quest for these objects has been hindered by the difficulty of detecting and identifying them; thus, very few examples are currently known. In this work we show how the combined high sensitivity and spatial resolution of the *Spitzer Space Telescope* and of the *Chandra X-Ray Observatory* are overcoming these difficulties, offering the capability of detecting and identifying heavily obscured AGNs up to high redshifts, providing constraints on their surface density, and characterizing their properties.

Using the data set in the *Chandra*/SWIRE field (0.6 deg^2 in the Lockman Hole), we conducted a search for Compton-thick AGNs. We selected, independently, two samples of Compton-thick AGN candidates based on their X-ray spectral properties and optical–IR SED. The X-ray– and IR-selected samples contain, respectively, five and 120 sources. Based on the properties of the X-ray–selected Compton-thick AGNs, we estimate that only 40% of the population of heavily obscured AGNs shows distinct AGN signatures in their optical–IR SEDs, the rest being dominated by the host galaxy emission. The number of Compton-thick AGNs detectable in the *Chandra*/SWIRE field is at least 25 sources deg^{-2}, and only 33% of them are detected in the X-ray

down to a flux limit of 10^{-15} ergs cm^{-2} s^{-1}. The X-ray/optical flux ratios of the selected obscured AGNs cover a similar range as the rest of the X-ray sample and well overlap with those observed for "classical" AGNs, indicating that searches for heavily obscured AGNs among X-ray sources with extreme X-ray/optical flux ratios might miss a large fraction of these sources.

The complete sample of AGNs selected on the basis of a red power-law–like IR SED contains 181 sources, of which 61 show SEDs similar to those of unobscured AGNs and 120 are obscured AGN candidates. The complete sample corresponds to only about 20% of the total number of AGNs expected to be detected in the mid-IR at our sensitivity. The observed ratio between obscured and unobscured AGNs is 2 : 1, still lower than the model predictions, $\sim$3 : 1. The estimated surface density of Compton-thick AGNs is only 10% of the expected value. These results suggest that even in the mid-IR, heavily obscured AGNs are elusive.

Optical spectroscopy of two obscured AGN candidates confirmed that they are high-redshift (SW 104409 at $z = 2.54$ and SW 104406 at $z = 2.43$), Compton-thick QSOs. These sources, characterized by type 2 AGN spectra, very red optical–IR SEDs, and high X-ray luminosities ($\sim 10^{45}$ ergs s^{-1}), have properties (SEDs, luminosities, and SMBH masses) similar to those observed in the high-z Compton-thick quasars CXO 52 ($z = 3.288$; Stern et al. 2002) and CDFS 202 ($z = 3.700$; Norman et al. 2002). However, they differ from submillimeter-selected Compton-thick AGNs (Alexander et al. 2005b), where emission from a starburst dominates at most wavelengths and black hole masses and accretion rates are 1 order of magnitude lower. SW 104409 represents the most luminous ($\sim 10^{14}\, L_{\odot}$) Compton-thick QSOs at high z currently known with an SMBH mass comparable to the most massive local SMBH ($\sim 3 \times 10^9\ M_{\odot}$). Such a rare object can be found when large volumes are sampled as in the *Chandra*/SWIRE field ($\sim$0.6 deg^2).

M. P. thanks Alain Omont and Dan Weedman for useful discussions. This work is based on observations made with the *Spitzer Space Telescope*, which is operated by the Jet Propulsion Laboratory, California Institute of Technology, under NASA contract 1407. Support for this work, part of the *Spitzer Space Telescope* Legacy Science Program, was provided by NASA through an award issued by the Jet Propulsion Laboratory, California Institute of Technology, under NASA contract 1407. M. P., B. W., and R. K. are grateful for the financial support of NASA grant G04-5158A (*Chandra*). B. W. is grateful for the financial support of NASA contract NAS8-39073 (*Chandra* X-Ray Center).

This research makes use of the NASA/IPAC Extragalactic Database (NED), which is operated by the Jet Propulsion Laboratory, California Institute of Technology, under contract with the National Aeronautics and Space Administration. This work is based on observations obtained at the Hale Telescope, Palomar Observatory, as part of a continuing collaboration between the California Institute of Technology, NASA/JPL, and Cornell University. This publication makes use of data products from the Two Micron All Sky Survey, which is a joint project of the University of Massachusetts and the Infrared Processing and Analysis Center/California Institute of Technology, funded by the National Aeronautics and Space Administration and the National Science Foundation.

Facilities: Spitzer (IRAC,MIPS), CXO (ACIS)

REFERENCES

Akiyama, M., Ueda, Y., Ohta, K., Takahashi, T., & Yamada, T. 2003, ApJS, 148, 275
Alexander, D. M., Bauer, F. E., Chapman, S. C., Smail, I., Blain, A. W., & Ivison, R. J. 2005a, ApJ, 632, 736
Alexander, D. M., Smail, I., Bauer, F. E., Chapman, S. C., Blain, A. W., Brandt, W. N., & Ivison, R. J. 2005b, Nature, 434, 738
Alexander, D. M., et al. 2001, ApJ, 554, 18
Alonso-Herrero, A., et al. 2004, ApJS, 154, 155
———. 2006, ApJ, 640, 167
Antonucci, R. 1993, ARA&A, 31, 473
Babbedge, T. S. R. 2004, Ph.D. thesis, Imperial College
Babbedge, T. S. R., et al. 2004, MNRAS, 353, 654
Barger, A., Cowie, L. L., Brandt, W. N., Capak, P., Garmire, G. P., Hornschemeier, A. E., Steffen, A. T., & Wehner, E. H. 2002, AJ, 124, 1839
Barger, A. J., Cowie, L. L., Mushotzky, R. F., Yang, Y., Wang, W.-H., Steffen, A. T., & Capak, P. 2005, AJ, 129, 578
Bassani, L., Dadina, M., Maiolino, R., Salvati, M., Risaliti, G., Della Ceca, R., Matt, G., & Zamorani, G. 1999, ApJS, 121, 473
Berta, S., Fritz, J., Franceschini, A., Bressan, A., & Pernechele, C. 2003, A&A, 403, 119
Bertin, E., & Arnouts, S. 1996, A&AS, 117, 393
Bolzonella, M., Miralles, J.-M., & Pelló, R. 2000, A&A, 363, 476
Borys, C., Smail, I., Chapman, S. C., Blain, A. W., Alexander, D. M., & Ivison, R. J. 2005, ApJ, 635, 853
Bouchet, P., Lequeux, J., Maurice, E., Prevot, L., & Prevot-Burnichon, M. L. 1985, A&A, 149, 330
Braito, V., et al. 2003, A&A, 398, 107
———. 2004, A&A, 420, 79
Calzetti, D., & Heckman, T. M. 1999, ApJ, 519, 27
Cattaneo, A., Blaizot, J., Devriendt, J., & Guiderdoni, B. 2005, MNRAS, 364, 407
Chapman, S. C., Blain, A. W., Smail, I., & Ivison, R. J. 2005, ApJ, 622, 772
Comastri, A. 2004, in Supermassive Black Holes in the Distant Universe, ed. A. J. Barger (Dordrecht: Kluwer), 245
Comastri, A., Brusa, M., & Mignoli, M. 2003, Astron. Nachr., 324, 28
Comastri, A., Setti, G., Zamorani, G., & Hasinger, G. 1995, A&A, 296, 1
Condon, J. J. 1988, in Galactic and Extragalactic Radio Astronomy, ed. G. L. Verschuur & K. I. Kellermann (2nd ed.; Berlin: Springer), 641
Cutri, R. M., Nelson, B. O., Francis, P. J., & Smith, P. S. 2002, in IAU Colloq. 184, ed. R. F. Green, E. Ye. Khachikian, & D. B. Sanders (ASP Conf. Ser. 284; San Francisco: ASP), 127
Cutri, R. M., et al. 2003, Explanatory Supplement to the 2MASS All Sky Data Release (Pasadena: Caltech), http://www.ipac.caltech.edu/2mass/releases/allsky/doc/explsup.html
Della Ceca, R., et al. 2004, A&A, 428, 383
De Luca, A., & Molendi, S. 2004, A&A, 419, 837
Dickey, J. M., & Lockman, F. J. 1990, ARA&A, 28, 215
Di Matteo, T., Springel, V., & Hernquist, L. 2005, Nature, 433, 604
Donley, J. L., Rieke, G. H., Rigby, J. R., & Pérez-González, P. G. 2005, ApJ, 634, 169
Dwelly, T., Page, M. J., Loaring, N. S., Mason, K. O., McHardy, I., Gunn, K., & Sasseen, T. 2005, MNRAS, 360, 1426
Efstathiou, A., & Rowan-Robinson, M. 1995, MNRAS, 273, 649
Elston, R., Rieke, G. H., & Rieke, M. J. 1988, ApJ, 331, L77
Elvis, M., et al. 1994, ApJS, 95, 1
Fabian, A. C. 1999, MNRAS, 308, L39
Fadda, D., Flores, H., Hasinger, G., Franceschini, A., Altieri, B., Cesarsky, C. J., Elbaz, D., & Ferrando, Ph. 2002, A&A, 383, 838
Fazio, G. G., et al. 2004, ApJS, 154, 10
Fiore, F., et al. 2003, A&A, 409, 79
Ford, H. C., et al. 2004, 1994, ApJ, 435, L27
Franceschini, A., et al. 2005, AJ, 129, 2074
Freeman, P. E., Doe, S., & Siemiginowska, A. 2001, Proc. SPIE, 4477, 76
Freeman, P. E., Kashyap, V., Rosner, R., & Lamb, D. Q. 2002, ApJS, 138, 185
Gallagher, S. C., Richards, G. T., Hall, P. B., Brandt, W. N., Schneider, D. P., & Vanden Berk, D. E. 2005, AJ, 129, 567
Granato, G., De Zotti, G., Silva, L., Bressan, A., & Danese, L. 2004, ApJ, 600, 580
Hao, L., et al. 2005, ApJ, 625, L75
Hatziminaoglou, E., et al. 2005, AJ, 129, 1198
Hopkins, P. F., Hernquist, L., Martini, P., Cox, T. J., Robertson, B., Di Matteo, T., & Springel, V. 2005, ApJ, 625, L71
Houck, J. R., et al. 2005, ApJ, 622, L105
Iwasawa, K., Matt, G., Guainazzi, M., & Fabian, A. C. 2001, MNRAS, 326, 894

Kim, D.-W., et al. 2004, ApJS, 150, 19
Kriss, G. A. 1994, in ASP Conf. Ser. 61, Astronomical Data Analysis Software and Systems III, ed. D. R. Crabtree, R. J. Hanisch, & J. Barnes (San Francisco: ASP), 437
Krolik, J. H. 1999, Active Galactic Nuclei: From the Central Black Hole to the Galactic Environment (Princeton: Princeton Univ. Press)
Lacy, M., et al. 2004, ApJS, 154, 166
La Franca, F., et al. 2005, ApJ, 635, 864
Longair, M. S. 1992, High Energy Astrophysics (Cambridge: Cambridge Univ. Press)
Lonsdale, C. J., et al. 2003, PASP, 115, 897
———. 2004, ApJS, 154, 54
Lutz, D., Maiolino, R., Spoon, H. W. W., & Moorwood, A. F. M. 2004, A&A, 418, 465
Madau, P. 1995, ApJ, 441, 18
Madau, P., Ghisellini, G., & Fabian, A. C. 1994, MNRAS, 270, L17
Mainieri, V., Bergeron, J., Hasinger, G., Lehmann, I., Rosati, P., Schmidt, M., Szokoly, G., & Della Ceca, R. 2002, A&A, 393, 425
Mainieri, V., et al. 2005, MNRAS, 356, 1571
Maiolino, R., & Rieke, G. H. 1995, ApJ, 454, 95
Maiolino, R., et al. 2003, MNRAS, 344, L59
Manners, J. C., et al. 2004, MNRAS, 355, 97
Martínez-Sansigre, A., Rawlings, S., Lacy, M., Fadda, D., Marleau, F. R., Simpson, C., Willott, C. J., & Jarvis, M. J. 2005, Nature, 436, 666
Massey, P., Strobel, K., Barnes, J. V., & Anderson, E. 1988, ApJ, 328, 315
Matt, G., Fabian, A. C., Guainazzi, M. Iwasawa, K., Bassani, L., & Malaguti, G. 2000, MNRAS, 318, 173
McLure, R. J., & Dunlop, J. S. 2004, MNRAS, 352, 1390
Moran, E. C., Filippenko, A. V., & Chornock, R. 2002, ApJ, 579, L71
Moretti, A., Campana, S., Lazzati, D., & Tagliaferri, G. 2003, ApJ, 588, 696
Morrison, R., & McCammon, D. 1983, ApJ, 270, 119
Nandra, K., & Pounds, K. A. 1994, MNRAS, 268, 405
Norman, C., et al. 2002, ApJ, 571, 218
Oke, J. B., et al. 1995, PASP, 107, 375
Osterbrock, D. E., & Shaw, R. A. 1988, ApJ, 327, 89
Padovani, P., Allen, M. G., Rosati, P., & Walto, A. 2004, A&A, 424, 545
Peeters, E., Spoon, H. W. W., & Tielens, A. G. G. M. 2004, ApJ, 613, 986
Perola, G. C., et al. 2004, A&A, 421, 491
Piccinotti, G., Mushotzky, R. F., Boldt, E. A., Holt, S. S., Marshall, F. E., Serlemitsos, P. J., & Shafer, R. A. 1982, ApJ, 253, 485
Piconcelli, E., Cappi, M., Bassani, L., Di Cocco, G., & Dadina, M. 2003, A&A, 412, 689
Polletta, M., Lonsdale, C. J., Xu, C., & Wilkes, B. J. 2003, Astron. Nachr., 324, 170
Prevot, M. L., Lequex, J., Prevot, L., Maurice, E., & Rocca-Volmerange, B. 1984, A&A, 132, 389
Richards, G. T., et al. 2003, AJ, 126, 1131
———. 2005, MNRAS, 360, 839
Rieke, G., et al. 2004, ApJS, 154, 25
Rigby, J. R., Rieke, G. H., Pérez-González, P. G., Donley, J. L., Alonso-Herrero, A., Huang, J.-S., Barmby, P., & Fazio, G. G. 2005, ApJ, 627, 134
Rigby, J. R., et al. 2004, ApJS, 154, 160
Rigopoulou, D., Spoon, H. W. W., Genzel, R. Lutz, D., Moorwood, A. F. M., & Tran, Q. D. 1999, AJ, 118, 2625
Risaliti, G., Maiolino, R., & Salvati, M. 1999, ApJ, 522, 157
Sanders, D. B., & Mirabel, I. F. 1996, ARA&A, 34, 749
Silk, J., & Rees, M. J. 1998, A&A, 331, L1
Silva, L., Maiolino, R., & Granato, G. L. 2004, MNRAS, 355, 973
Smith, D. A., & Done, C. 1996, MNRAS, 280, 355
Smith, P. S., Schmidt, G. D., & Hines, D. C. 2003, ApJ, 593, 676
Spergel, D. N., et al. 2003, ApJS, 148, 175
Springel, V., Di Matteo, T., & Hernquist, L. 2005, MNRAS, 361, 776
Stern, D., et al. 2002, ApJ, 568, 71
———. 2005, ApJ, 631, 163
Surace, J. A., et al. 2005, SWIRE Data Delivery Document II, *Spitzer* Science Center (Pasadena: Caltech)
Szokoly, G. P., et al. 2004, ApJS, 155, 271
Tadhunter, C., Marconi, A., Axon, D., Wills, K., Robinson, T. G., & Jackson, N. 2003, MNRAS, 342, 861
Treister, E., & Urry, C. M. 2005, ApJ, 630, 115
Treister, E., et al. 2004, ApJ, 616, 123
Ueda, Y., Akiyama, M., Ohta, K., & Miyaji, T. 2003, ApJ, 598, 886
Urrutia, T., Lacy, M., Gregg, M. D., & Becker, R. H. 2005, ApJ, 627, 75
Van Duyne, J., et al. 2004, BAAS, 205, 163.09
van Dyk, D. A., Park, T., Kashyap, V. L., & Zezas, A. 2004, BAAS High Energy Astrophys., 8, 1627
Vignati, P., et al. 1999, A&A, 349, L57
Webster, R. L., Francis, P. J., Peterson, B. A., Drinkwater, M. J., & Masci, F. J. 1995, Nature, 375, 469
Weedman, D. W., et al. 2005, ApJ, 633, 706
Weisskopf, M. C., O'dell, S. L., & van Speybroeck, L. P. 1996, Proc. SPIE, 2805, 2
Werner, M. W., et al. 2004, ApJS, 154, 1
White, R. L., Helfand, D. J., Becker, R. H., Gregg, M. D., Postman, M., Lauer, T. R., & Oegerle, W. 2003, AJ, 126, 706
Wilkes, B. J., Schmidt, G. D., Cutri, R. M., Ghosh, H., Hines, D. C., Nelson, B., Smith, & Paul, S. 2002, ApJ, 564, L65
Wilson, J. C., et al. 2003, Proc. SPIE, 4841, 451
Wolf, C., Wisotzki, L., Borch, A., Dye, S., Kleinheinrich, M., & Meisenheimer, K. 2003, A&A, 408, 499
Worsley, M. A., Fabian, A. C., Barcons, X., Mateos, S., Hasinger, G., & Brunner, H. 2004, MNRAS, 352, L28
Worsley, M. A., Fabian, A. C., Bauer, F. E., Alexander, D. M., Hasinger, M. S., Brunner, H., Brandt, W. N., & Schneider, D. P. 2005, MNRAS, 357, 1281
Xu, C., Lonsdale, C. J., Shupe, D. L., Franceschini, A., Martin, C., & Schiminovich, D. 2003, ApJ, 587, 90
Zakamska, N. L., Strauss, M. A., Heckman, T. M., Ivezic, Z., & Krolik, J. H. 2004, AJ, 128, 1002